

Multifaceted activation of STING axis upon Nipah and Measles virus-induced syncytia formation

Lucia Amurri

CIRI, Centre International de Recherche en Infectiologie

Claire Dumont

INSERM https://orcid.org/0000-0001-7511-1512

Rodolphe Pelissier

CIRI, Centre International de Recherche en Infectiologie

Olivier Reynard

International Center for Infectiology Research https://orcid.org/0000-0001-7536-355X

Cyrille Mathieu

CIRI, Centre International de Recherche en Infectiologie, Team Immuno-Biology of Viral Infections, Univ Lyon, Inserm, U1111, Université Claude Bernard Lyon 1, CNRS, UMR5308, ENS de Lyon https://orcid.org/0000-0002-6682-2029

Julia Spanier

Institute for Experimental Infection Research, TWINCORE https://orcid.org/0000-0002-8797-3563

Bernadett Pályi

National Public Health Center

Daniel Deri

National Biosafety Laboratory, National Center for Public Health and Pharmacy

Ludovic Karkowski

CIRI, Centre International de Recherche en Infectiologie

Jennifer Skerra

Center for Experimental and Clinical Infection Research

Zoltán Kis

National Public Health Center

Ulrich Kalinke

TWINCORE, Centre for Experimental and Clinical Infection Research

Branka Horvat

INSERM https://orcid.org/0000-0003-0578-7765

CIRI, Centre International de Recherche en Infectiologie https://orcid.org/0000-0002-8946-3049

Article

Keywords:

Posted Date: January 17th, 2024

DOI: https://doi.org/10.21203/rs.3.rs-3837372/v1

License: © ① This work is licensed under a Creative Commons Attribution 4.0 International License.

Read Full License

Additional Declarations: There is NO Competing Interest.

Abstract

Activation of the DNA-sensing STING axis by RNA viruses plays a role in antiviral response through mechanisms that remain poorly understood. Here, we show that the STING pathway regulates Nipah virus (NiV) replication *in vivo* in mice. Moreover, we demonstrate that following both NiV and measles virus (MeV) infection, IFNγ-inducible protein 16 (IFI16), an alternative DNA sensor in addition to cGAS, induces the activation of STING, leading to the phosphorylation of NF-κB p65 and the production of IFNβ and interleukin 6. Finally, we found that paramyxovirus-induced syncytia formation is responsible for loss of mitochondrial membrane potential and leakage of mitochondrial DNA in the cytoplasm, the latter of which is further detected by both cGAS and IFI16. These results contribute to improve our understanding about NiV and MeV immunopathogenesis and provide potential paths for alternative therapeutic strategies.

Introduction

Innate immunity plays a critical role in antiviral responses, and cyclic quanosine monophosphateadenosine monophosphate (cGAMP) synthase/stimulator of IFN genes (cGAS/STING) is the main innate immune signaling axis involved in the recognition of cytoplasmic double-strand DNA (dsDNA) 1. The STING pathway can be activated by both non-self-DNA of invading pathogens and self-DNA derived from damaged organelles in cancerous, senescent or infected cells ²⁻⁴. In the presence of immunostimulatory DNA, the sensor cGAS binds the minor groove of dsDNA in a sequence-independent manner through its zinc-ion-binding domain, thus oligomerizing and catalyzing the synthesis of cyclic dinucleotide cGAMP ^{5,6}. Then, cGAMP acts as a second messenger by binding and activating STING, inducing its oligomerization and translocation from the endoplasmic reticulum (ER) to the Golgi apparatus and the perinuclear puncta 7. There, STING is phosphorylated by TANK-binding kinase 1 (TBK1), resulting in the recruitment of interferon (IFN) regulatory factor 3 (IRF3) and the induction of type I IFNs (IFN-I) and other cytokines ⁸⁻¹². While being identified as a major actor in the sensing of exogenous pathogenic DNA, the STING axis also plays an important role in the response against various enveloped RNA viruses, such as flaviviruses, coronaviruses and orthomyxoviruses, through indirect mechanisms, as previously described ^{13,14}. In addition, we have recently demonstrated the involvement of the STING axis in the control of Nipah (NiV) and measles virus (MeV) infection ^{15,16}, although the mechanism of virus-induced activation of STING axis remained unclear.

NiV and MeV are both *Mononegavirales* belonging to the *Paramyxoviridae* family, which is characterized by an enveloped virion containing a non-segmented single-stranded RNA (ssRNA) genome of negative polarity ^{17,18}. NiV is an emerging highly pathogenic virus mainly transmitted through the respiratory or oral route by *Pteropus* fruit bats, which are widespread in South-East Asia, Australia and Africa and constitute an asymptomatic host reservoir ^{19,20}. The symptoms of Nipah disease include severe pneumonia and encephalitis with up to 100% lethality and no vaccine or therapeutic against NiV are currently available. In addition, several factors, such as intensive farming and global warming, can

contribute to an uncontrolled spreading of this virus with pandemic potential ²¹. Indeed, NiV is classified among chemical, radiological, biological and nuclear threats and belongs to the World Health Organization Blueprint list of priority pathogens for research and development, underlying the urge to improve our understandings on NiV immunopathogenesis to develop innovative therapeutic strategies.

MeV is a highly contagious reemerging virus transmitted through the respiratory route. Measles disease symptoms are ranging from mild (fever, cough, skin rash and conjunctivitis) to severe (pneumonia and encephalitis) ²². Moreover, due to its ability to infect immune cells, MeV induces a transient immune suppression known as "immune amnesia", thus increasing the risk of opportunistic infections ^{23,24}. Despite the availability of a safe and effective vaccine, measles outbreaks are resurging in recent years due to a suboptimal vaccination coverage, which has been worsened by the delay in routine children vaccinations during COVID-19 pandemic ^{25,26}. While NiV glycoprotein (G) binds cellular ephrin B2 and B3 receptors, which are ubiquitously expressed and highly conserved in mammalians ²⁷, MeV hemagglutinin (H) interacts with CD150 and Nectin-4 receptors expressed on immune and epithelial cells, respectively ^{28–30}. In addition, MeV H from vaccinal strains also interacts with the ubiquitously expressed CD46 receptor ^{31,32}. The expression of G/H and fusion (F) envelope glycoproteins on the surface of infected cells during viral replication induces cell-to-cell fusion, leading to the formation of multinucleated giant cells named syncytia both *in vitro* and *in vivo* ^{33,34}.

We have recently demonstrated that Paramyxovirus infection activates STING axis both in vitro and in vivo along canonical RNA sensors such as Toll-like receptors (TLR) and RIG-l-like receptors (RLR) 15,16. We observed a synergistic and non-redundant role of STING together with mitochondrial antiviral signaling protein (MAVS) and myeloid differentiation primary response 88 (MyD88) in the control of NiV infection in mice 16. Moreover, Sato et al. recently observed that virus-induced downregulation of mitochondrial biogenesis triggers the release of mitochondrial DNA (mtDNA) in the cytoplasm and activates cGAS during MeV infection³⁵. STING can undergo non-degradative K63-linked ubiquitination by multiple E3 ubiquitin ligases, such as tripartite motif containing protein 32 (TRIM32), TRIM56 or tumor necrosis factor receptor-associated factor 6 (TRAF6), resulting in the induction of nuclear factor kappa B (NF-κB) and subsequent expression of inflammatory cytokines ³⁶⁻³⁸. In addition to cGAS, another DNA sensor, IFNy inducible protein 16 (IFI16), has been described as an alternative activator of STING ^{39,40}. IFI16 binds damaged DNA through its hematopoietic expression-IFN inducible-nuclear localization (HIN) domain and activates STING through a cGAMP-independent mechanism in complex with tumor suppressor p53 and TRAF6 40,41. While cGAMP predominantly induces STING phosphorylation and triggers IFN-I expression through TBK1 and IRF3, IFI16-dependent STING activation is associated to a prevalence of poly-ubiquitinated STING and NF-κB activation ^{40,42}. Thus, deciphering the function of the different stimulators of STING is fundamental to understand the impact on STING axis activation and further gene expression.

Here, we report that, concomitantly to our previous observations ¹⁶, the deficiency of STING (knock out, KO) affects the control of NiV infection in mice *in vivo*. Indeed, our animal experiment revealed an

increase in viral replication that is associated with a decrease in CXC motif chemokine ligand 10 (CXCL10) expression and impaired production of neutralizing antibodies in KO animals compared to the wild-type (WT). We have then investigated the cellular and molecular profiles associated with STING activation during *Paramyxovirus* infection *in vitro* and showed that STING is activated in parallel through two distinct and independent mechanisms. While the canonical cGAS/STING pathway is mainly involved in the implementation of the IFN-I response, the non-canonical axis involving IF116 has a prevalent effect on STING-dependent activation of NF-κB subunit p65, mainly responsible for inflammatory cytokines' expression. Moreover, our results revealed that STING activation is dependent on virus-induced membrane fusion following both NiV and MeV infection. Finally, we demonstrate that syncytia formation triggers mitochondrial loss of membrane potential in infected cells and the release of mtDNA in the cytoplasm, which is further sensed by both cGAS and IF116. Overall, our study highlights novel aspects of STING axis activation during RNA virus infections and provides key elements to better understand immunovirological mechanisms involved during *Paramyxovirus* infection.

Results

STING plays a role in the control of NiV infection in mice

While our previous study demonstrated a synergistic role of STING in addition to RNA-sensing axes of innate immunity, namely TLR/MyD88 and RLR/MAVS pathways 16, the impact of STING alone on NiV infection in vivo remained unknown. Therefore, we compared the infection with NiV-Malaysia in wild-type (WT), IFNα/β receptor (IFNAR) KO and STING KO mice for 28 days (Fig. 1). While all WT mice survived NiV infection without developing disease, as previously described 43, 5 out of 6 IFNAR KO mice died following infection. Similarly to WT mice, all STING KO mice survived the NiV challenge without developing clinical symptoms (Fig. 1A). However, despite their survival, the neutralizing antibodies titer in the serum of STING KO mice was equivalent to IFNAR KO mice that reached endpoint euthanasia and significantly reduced compared to WT (Fig. 1B). Then, to further characterize the impact of STING in the control of NiV infection, we harvested lung, spleen and brain of mice at early (day 0-day 2), mid (day 2day 7), or late (day 7-day 28) phase of infection and analyzed viral replication and cytokine expression by RT-qPCR and immunofluorescence (Fig. 1C, D). CXCL10 is known to be an important chemo-attractant involved in the generation of inflammatory immune response and overexpressed during NiV infection 44. Although the lack of STING did not affect animal survival and despite similar levels of IFNB mRNA, STING KO mice displayed significantly higher viral NiV-N mRNA levels followed by lower expression of CXCL10 in the mid phase of infection compared to WT mice in all tested organs (Fig. 1C). Moreover, viral replication, CXCL10 mRNA levels and thus response of STING KO mice were intermediate in between WT and IFNAR KO mice (Fig. 1C). These observations were confirmed at a viral level, as we detected more NiV N protein in all organs harvested from STING KO mice compared to WT mice at mid phase of infection, thus representing the peak of infection (Fig. 1C, D). Overall, these results demonstrate an important role of STING axis in the control of NiV infection *in vivo* thus confirming the involvement of this DNA sensor in parallel to RNA-sensing pathways.

STING pathway controls both IFN-I and NF-kB responses following NiV infection

To investigate how STING pathway regulates the innate immune response to NiV infection in human main cellular targets, we analyzed modulation of IFN-I through IFNβ expression and NF-κB p65 activation in human pulmonary microvascular endothelial cells (HPMEC) infected with recombinant NiV-eGFP and treated or not with a specific STING inhibitor (H-151) or cGAS inhibitor (RU.521) (Fig. 2). NiV infection induced the activation of STING through phosphorylation, as observed by fluorescent microscopy, while H151 and RU.521 treatments strongly reduced phospho-STING (p-STING) staining at similar levels (Fig. 2A). Also, we determined that NiV infection was associated with a significant increase in IFNβ expression, which was decreased by both H151 and RU.521 treatments, demonstrating a STING-dependent IFNβ induction in response to NiV (Fig. 2B).

In parallel, we evaluated activation of NF-κB p65 subunit and observed its nuclear translocation following NiV infection, that was significantly reduced by both H-151 and RU.521 treatments (Fig. 2C, D). However, contrary to what occurred for p-STING where its levels decreased drastically, cGAS specific inhibition through RU.521 had a significantly lower effect on the inhibition of p65 nuclear translocation, compared to STING inhibition by H-151 (Fig. 2D), suggesting an alternative stimulus for NF-κB pathway. Altogether, these data indicate that STING pathway contributes to trigger both IFN-I and NF-κB responses following NiV infection. Moreover, our data suggested that a non-canonical cGAS-independent stimulus is also involved in the activation of NF-κB pathway, thus implying the participation of an alternative DNA sensor during NiV infection.

STING-associated sensors cGAS and IFI16 are involved in the control of NiV and MeV infection

To further analyze a possible role of an alternative STING-activating DNA sensor during NiV and MeV infection, we investigated the potential contribution of IFI16 as a DNA sensor in parallel to cGAS. Indeed, we previously demonstrated that STING undergoes non-degradative K63-linked ubiquitination following NiV and MeV infection ¹⁶ and IFI16 was shown to predominantly trigger STING ubiquitination ⁴⁰. To address the role of each factor in the innate response against viral infection, we infected susceptible monocytic THP-1 cells WT or K0 for STING, cGAS or IFI16 with NiV-eGFP (Fig. 3A, B) or MeV-eGFP (Fig. 3C, D). Our data demonstrated an increased viral propagation in cell cultures lacking each analyzed molecule involved in the sensing of DNA, compared to WT cells (Fig. 3A, C and S1A, B). Moreover, our flow cytometry data were further confirmed by RT-qPCR, demonstrating that NiV-N and MeV-N RNA levels were significantly increased in STING KO, cGAS KO and IFI16 KO cells compared to WT THP-1 cells (Fig. 3B, D). Overall, these results determined the involvement of IFI16 along cGAS in the control of NiV and MeV infections by STING axis.

cGAS promotes phosphorylation of STING and IFI16 favors NF-кВ p65 activation following NiV and MeV infection

To investigate whether cGAS and IFI16 could differently activate STING and its subsequent pathway, we analyzed protein levels of p-STING and phospho-p65 NF-κB (p-p65), along with IFNβ and IL-6 mRNA levels in WT, STING KO, cGAS KO and IFI16 KO THP-1 cells infected with either NiV-eGFP (Fig. 4A-C) or MeV-eGFP (Fig. 4D-F). These targets were chosen in an attempt to dissect two separate axes of STING activation: one canonical axis mainly involving cGAS/p-STING/IFNB and the other non-canonical axis mostly represented by IFI16/p-p65/IL-6. First, to maximize virus-induced signaling activation we verified that all our cultures were efficiently infected by following eGFP immunofluorescence (Fig. 4A, D). Western blot analyses then demonstrated that p-STING and p-p65 levels were strongly increased in NiV- and MeVinfected WT cells compared to uninfected cultures (Fig. 4B, E). In addition, our data confirmed that STING is involved in the activation of NF-kB p65 following NiV and MeV infection as STING KO cultures displayed reduced levels of p-p65 compared to WT cells (Fig. 4B, E). Interestingly, cGAS KO and IFI16 KO presented opposite effects on STING and NF-kB p65 activation following both NiV and MeV infection. Though the absence of cGAS had a strong impact in reducing p-STING levels while p-p65 remained high. the lack of IFI16 generated an important diminution of p-p65 levels while maintaining a relatively high amount of p-STING (Fig. 4B, E). These observations were corroborated also at cytokine levels, as both IFNβ and IL-6 mRNA amounts were increased in WT THP-1 cultures following NiV and MeV infection (Fig. 4C, F). Moreover, both cytokines' levels were significantly reduced in the absence of STING confirming its global action in cytokine response to paramyxoviruses. Finally, while cGAS KO THP-1 cells displayed an important reduction in IFNB mRNA levels and relatively maintained IL-6 amounts, IFI16 KO THP-1 cells exerted opposite effects with relative decrease of IFNB mRNA quantity and a major reduction in IL-6 mRNA levels (Fig. 4C, F). Altogether, these data confirm the presence of two parallel axes involved in the activation of STING pathway following *Paramyxovirus* infections, where cGAS mostly favors STING phosphorylation and IFN-I response, while IFI16 mainly triggers NF-kB activation and proinflammatory cytokines response possibly through STING ubiquitination as previously described ^{16,40}.

Virus-induced syncytia lead to STING activation and expression of IFN-I and inflammatory cytokines

Since STING activation occurs during *Paramyxovirus* infections in the absence of a viral DNA agonist, we hypothesized that virus-induced perturbations of cellular homeostasis could represent a danger signal triggering STING axis through endogenous DNA, as observed in numerous other RNA virus and bacterial infections^{45–47}. To identify a potential mechanism responsible for this phenomenon, we investigated whether syncytia formation could be associated with STING activation. To address its role, we infected HPMEC cells with NiV-eGFP (Fig. 5A, B) or MeV-eGFP (Fig. 5C, D) and cells were mock-treated or treated with virus-specific fusion inhibitory peptides so called VIKI-PEG4-Chol (VIKI), derived from Human Para-influenza virus 3, and HRC4, derived from MeV, respectively, 6 h post infection, thus allowing cell infection but preventing virus-induced cell-to-cell fusion ^{48–50} (Fig. 5A, C). p-STING was significantly increased in infected mock-treated cells as observed by western blot analyses, while STING phosphorylation was strongly reduced in infected cells treated with fusion inhibitory peptides (Fig. 5B, D and S2A, B),

suggesting that syncytia formation could be responsible for STING activation during NiV and MeV infection.

To analyze whether the sole viral syncytia formation is sufficient for an induction of STING response, in the absence of other virus-induced stress factors, we transfected 293T cells, that do not express STING or IFI16 and display weak cGAS levels, with plasmids coding for NiV-F and/or G envelope glycoproteins (Figure S2C, D) and eGFP. Then, 293T were self-cultured or co-cultured with 293 cells expressing all proteins involved in STING pathway (Fig. 5E, S2D). First, we observed that despite syncytia formation in 293T cultures, no cytokine induction was observed (Fig. 5F, G, H, I). Then, we demonstrated that despite co-culture between 293T and 293 cells, no increase of IFNβ, IL-6 and CXCL-10 mRNA expression occurred in any condition that did not present syncytia, including mock-, single NiV F- or single NiV-G-transfected 293T cells (Fig. 5F, G, H, I). Finally, our results highlighted that syncytia formation detected following coculture of double NiV F/NiV G-transfected 293T with 293 cells triggered the expression of IFNβ, IL-6 and CXCL-10 cytokines that were all inhibited in the presence of VIKI fusion inhibitory peptides (Fig. 5F, G, H, I). Overall, our data proved that cell-cell fusion perpetrated by NiV envelope glycoproteins is responsible for the STING-dependent induction of cytokine expression.

STING axis pathway activation is associated with mitochondrial stress and DNA damage following paramyxovirus-induced syncytia formation

We next aimed at identifying a potential intracellular perturbation responsible for STING pathway activation following NiV and MeV infection. As it was recently published that mitochondrial stress occurs during MeV infection leading to leakage of mitochondrial DNA (mtDNA) in the cytoplasm and further sensing by cGAS³⁵, we investigated whether mitochondrial dysfunction and STING activation could be associated to syncytia formation. HPMEC cells infected with NiV-eGFP (Fig. 6A-C) or MeV-eGFP (Fig. 6D-F) and treated or not with VIKI or HRC4 fusion inhibitory peptides, respectively, were stained with an antip-STING antibody and Mitotracker Orange CM-H2TMRos dye. Mitotracker is a mitochondrion-selective fixable live dye that penetrates in actively respiring cells, where it is oxidized and sequestered in mitochondria ⁵¹. Infected cells displayed a significant decrease in Mitotracker intensity (Fig. 6B, E), thus indicating a reduction in mitochondrial membrane potential that can be associated with mitochondrial dysfunction. In parallel, p-STING was detected in perinuclear areas in both NiV- and MeV-infected cells (Fig. 6C, F). In contrast, Mitotracker and p-STING intensity in infected cells treated with fusion inhibitory peptides were equivalent to the non-infected condition (Fig. 6B, C, E, F). These results show that both mitochondrial stress and STING activation occur in *Paramyxovirus*-induced syncytia.

To confirm that virus-induced cell-cell fusion is responsible for these observed effects, we cultured HeLa cells WT or stably expressing NiV-F or NiV-G envelope glycoproteins either alone or in co-culture in the presence or absence of VIKI fusion inhibitory peptides (Fig. 6G-J and S3A). The correct expression of NiV-F and G was verified by flow cytometry (Figure S3B). Our results showed that Mitotracker intensity levels were reduced, and p-STING levels were increased when HeLa-NiV-F and HeLa-NiV-G were co-cultured compared to WT HeLa and self-cultured HeLa-NiV-F or HeLa-NiV-G. Moreover, these effects were reverted

by the presence of fusion inhibitory peptides, thus confirming the involvement of paramyxovirus envelope glycoproteins (Fig. 6G-J). Additionally, we observed in the co-culture an increased staining of the phosphorylated histone 2AX (p-H2AX), a marker of double strand breaks (DSB) indicating DNA damage (Fig. 6G), and relocalization of both nuclear and cytoplasmic cGAS to perinuclear areas (Fig. 6H) and both effects were prevented in fusion peptide-treated conditions. In contrast, no change in the subcellular localization of IFI16 was observed, as IFI16 remained intranuclear in all conditions (Fig. 6I). Overall, these results demonstrate that viral-induced syncytia trigger mitochondrial stress and STING activation, together associated with DNA damage and the presence of both cGAS and IFI16 nuclear-associated location.

Mitochondrial DNA is responsible for STING activation through its sensing by both cGAS and IFI16 during NiV and MeV infection.

We finally investigated intracellular agonists that could be involved in the activation of STING axis. As previously shown, cGAS detects cytosolic mtDNA during MeV infection 35, thus we extended our analysis to NiV and considered the potential role of IFI16. To study whether IFI16 contributes to the detection of cytoplasmic endogenous DNA in parallel to cGAS following syncytia formation, we performed a coimmunoprecipitation experiment on WT HeLa cells infected with NiV-eGFP (Fig. 7A, C, E and S4A) or MeVeGFP (Fig. 7B, D, F and S4A) in the presence or absence of VIKI or HRC4 fusion inhibitory peptides. respectively. Both cGAS and IFI16 proteins were immunoprecipitated from cytoplasm extracts (Fig. 7A, B) and potential DNA bound to cGAS and IFI16 was analyzed by qPCR with mtDNA- or nuclear DNA-specific primers (Fig. 7C-F and S4C-F). First, we verified that our selected target genes were amplified by our couples of primers in HeLa cells by qPCR (Figure S4B). A significant increase in mtDNA coimmunoprecipitated with cGAS was measured following NiV and MeV infection (Fig. 7C, D), confirming previous observations ³⁵. In addition, immunoprecipitated IFI16 as well resulted to be enriched in mtDNA following infection (Fig. 7E, F). Moreover and concomitant to previous data, no nuclear DNA was detected neither in cGAS nor in IFI16 immunoprecipitation (Figure S4B-E) 35. Furthermore, the levels of mtDNA coimmunoprecipitated with cGAS and IFI16 were significantly reduced in infected cells treated with fusion inhibitor peptides compared to non-treated infected condition (Fig. 7C-F). Altogether, these results strongly suggest that, following *Paramyxovirus* infection and the subsequent syncytia formation, mtDNA is released in cytoplasm and represents the main cellular agonist detected by both cGAS and IFI16 and responsible for the activation of STING axis (Fig. 8).

Discussion

Our previous work highlighted that DNA-sensing STING pathway is involved in the response against NiV and MeV infection ^{15,16}. However, the precise role of STING and the cellular mechanisms responsible for its activation during *Paramyxovirus* infection remained obscure and needed further investigations.

To clarify the role of STING *in vivo*, we infected WT, IFNAR KO and STING KO mice with NiV and monitored animal survival, viral replication and cytokine expression for 28 days. We observed that the

absence of STING alone did not impair animal survival, as in STING KO mice TLR and RLR signaling pathways which are primarily responsible for viral RNA detection remained fully expressed. However, STING deletion resulted in a higher viral load and lower CXCL10 expression in KO animals compared to WT mice. Furthermore, a compromised STING response could have an impact on humoral adaptive immunity, as previously described ^{52,53}, as suggested by the fact that STING KO mice displayed significantly lower neutralizing antibodies titers compared to WT mice. As a consequence, it would be interesting to test whether a treatment with specific STING agonists, alone or as vaccine adjuvant, could contribute to boost both innate and adaptive immune responses against NiV infection ⁵⁴.

While we previously focused on the activation of IFN-I production, we later observed that both IFN-I and NF-kB responses are induced in a STING-dependent manner after NiV infection. Interestingly, cGAS appeared to be more important in the activation of IFN-I rather than NF-kB, leading us to hypothesize the presence of an alternative DNA sensor mainly involved in the trigger of STING-dependent NF-kB signalling in parallel to cGAS. As IFI16 was demonstrated to initiate non-canonical STING activation mainly through ubiquitination followed by subsequent NF-kB induction, in opposition to the canonical cGAS/cGAMP/STING/IRF3 pathway, we tested the implication of IFI16 in the immune response to Paramyxovirus infection ⁴⁰. We observed that IFI16 is involved in the control of viral replication following both NiV and MeV infection and has a major effect on NF-kB p65 phosphorylation downstream STING. Thus, these results confirm the model with two parallel axes of STING pathway, one involving cGAS followed by a major induction of STING phosphorylation and subsequent IFN-I response, the other represented by IFI16 mainly leading to NF-κB p65 nuclear translocation ⁴⁰. However, it remains obscure whether these two axes are independent or if there is competition, synergy or crosstalk between them. It has been shown that IFI16 can contribute to IFN-I induction through the activation of STING and TBK1 to enhance cGAMP-dependent activation of STING in macrophages, however it is unknown whether the same phenomenon occurs during NiV and MeV infection ⁵⁵. Understanding the interaction among the two pathways would be of great interest, as they could play an important role in antiviral immune regulation.

To decipher viral-dependent cellular mechanisms associated to STING activation we addressed the involvement of syncytia, the most important cytopathic effect perpetrated by both NiV and MeV, as the formation of multi-nucleated giant cells had been previously associated to the non-canonical activation of STING ^{47,46}. We observed that virus-induced cell-cell fusion triggers the phosphorylation of STING *in vitro*, supporting the previous finding that MeV-induced fusion amplifies IFN-I response ⁵⁶. However, we cannot exclude that additional virus-induced danger signals could contribute to STING activation, with possible differences according to viral strains and/or target cell types. Moreover, it was previously described that MeV infection induces mitochondrial stress through the downregulation of mitochondrial biogenesis and that V protein of MeV can damage the mitochondrial network by interacting with delta-aminolevulinate synthase 1 (ALAS1) ^{35,57}. We confirmed in this work that a reduction in mitochondrial membrane potential occurs following both NiV and MeV infection and we extended our demonstration that it is triggered through a fusion-dependent process. Nonetheless, the mechanism linking syncytia formation to mitochondrial stress remains unknown and further investigations are required. Moreover, we

showed here that STING phosphorylation is triggered in THP-1 monocytic cell line despite minimal syncytia formation. This could be due to the co-existence of multiple mechanisms of STING activation with possible variations according to different cell types.

Finally, we observed that, following NiV and MeV infection, mtDNA is released in the cytoplasm through a syncytia-dependent mechanism and sensed by both cGAS and IFI16, confirming that STING is both canonically and non-canonically activated by endogenous DNA during *Paramyxovirus* infection. Despite the fact that nuclear DNA was not detected along mtDNA released in the cytoplasm, we cannot exclude that genomic DNA might participate in STING activation through uncharacterized mechanisms. Moreover, while NiV infection induced a 100-fold increase of mtDNA co-immunoprecipitated with cytoplasmic cGAS and IFI16 compared to non-infected cells, only a less-than 10-fold mtDNA enrichment was observed following MeV infection, which could lead to a different potency of STING activation and possible consequences on inflammatory cytokine and IFN-I production. This could be due to the fact that viral loads in non-treated NiV-infected samples were higher compared to treated infected samples, while these differences were not observed in MeV-infected cells (Figure S4A), underlying a different speed in viral replication *in vitro* between these two paramyxoviruses.

It is interesting to note that NiV and MeV induce the activation of the STING axis in human cells despite the fact that this signaling pathway is detrimental for viral growth. Moreover, differently from what was observed for other RNA viral families, such as *Flaviviridae* and *Coronaviridae* ¹³, no viral protein of NiV has been shown to antagonize the STING axis yet. This could be a consequence of the fact that humans represent an accidental host for NiV, whose natural reservoir is the fruit bat. Bats have a dampened STING response, which prevents a STING-dependent hyper-inflammation that would derive from the high amount of cytosolic DNA generated through metabolic stress during flight activity ⁵⁸. This could contribute to explain the ability of these mammals to host NiV, which is highly pathogenic for humans, without developing symptoms. Thus, it would be interesting to compare human and bat STING pathway responses following *Paramyxovirus* infection to clarify a possible link between STING over-activation and pathogenicity in humans.

It has been demonstrated that other RNA viruses, such as Dengue virus, trigger STING activation through mitochondrial damage induction ⁵⁹, or through the generation of syncytia, as observed in SARS-CoV-2 infection ⁴⁶, but no connection between syncytia formation and mitochondrial damage was established before our work. We suggest that it could be useful to test these mechanisms in the context of other RNA virus infections to understand whether this could represent a conserved pattern of STING activation.

In conclusion, we demonstrate that during NiV and MeV infection, the STING pathway is activated through the recognition of leaked mtDNA detected by both cGAS and IFI16 following the formation of syncytia, leading to the subsequent expression of both IFN-I and inflammatory cytokines. Its important role in the control of NiV and MeV infection *in vitro* and *in vivo* suggests the credible employment of STING-targeting molecules as promising therapeutic strategies to treat *Paramyxovirus* infections.

Materials and Methods

Ethical statement

Animal experiments in the BSL-4 of Budapest were performed according to the guidelines of the European Communities Council Directive (86/609 EEC) and were approved by the Hungarian National Authority (PE/EA/1456-7/2020).

Animals in transit at Plateau de Biologie experimentale de la souris (PBES) in Lyon were manipulated in accordance to good experimental practice and approved by the regional ethics committee CECCAPP and authorized by the French Ministry of Higher Education and Research (no. 00962.01).

Viruses

NiV-Mal (isolate UMMC1 GenBank- AY029767), recombinant NiV (rNiv)—enhanced green fluorescent protein (eGFP) (Yoneda et al., 2006) and recombinant MeV IC323 vaccine strain, expressing Edmonston H and eGFP (Hashimoto et al., 2002), kindly provided by Dr Y. Yanagi (Kyushu University, Japan) and were prepared by infecting Vero-E6 cells (ATCC), in the INSERM Jean Mérieux biosafety level 4 (BSL-4) and BSL-2 laboratories at CIRI in Lyon, France respectively.

Mice

Wild type (WT) C57BL/6J mice (Charles River), B6.129S2-Ifnar1^{tm1(Neo)Agt} (IFNAR-KO) ⁶⁰ and B6(Cg)-Tmem173tm1.2Camb/J (Tmem173^{-/-}, STING KO) ⁶¹ mice were bred under specific pathogen-free conditions in the central mouse facility of the Helmholtz Centre for Infection Research, Brunswick, and at TWINCORE, Centre for Experimental and Clinical Infection Research, Hanover, Germany. Mouse experimental work was carried out using 4-week-old to 6-week-old mice and sex balance between male and female was respected.

Intraperitoneal infection of mice

All work with live Nipah Virus Malaysian Strain (NiV-Mal) was performed under BSL-4 conditions at the National Biosafety Laboratory at the National Center for Public Health and Pharmacy in Budapest, Hungary. All mice were inoculated intraperitoneally with 10⁶ TCID50 NIV-Mal under inhalational anesthesia with isoflurane (isoflurane: ISOFLUTEK 1000 mg/g, Laboratorios Karizoo S.A.; anesthesia station: MiniHUB-V3, TEM SEGA, France).

Sample collection and preparation

Euthanasia with CO₂ was conducted under inhalational anesthesia with isoflurane as well, followed by blood collection via cardiac puncture, and autopsy. During autopsy collection of brain, lung and spleen tissue were performed for further nucleic acid isolation and immunohistochemistry. Organs were divided for molecular testing and were collected and freezed immediately on -80°C without any medium until

further preparation. Parts of organs for immunohistochemistry were collected into fixative 10 V/V% formaldehyde-PBS solution. Then, 25–30 mg of the thawed organs were taken into MagNA Lyser Green Beads tubes (Roche Diagnostics GmbH, Mannheim, Germany) containing 600 μ L of 1:101 mixture of β -mercaptoethanol and Buffer RLT (QIAGEN GmbH, Hilden, Germany). After homogenisation using MagNA Lyser instrument (Roche Diagnostics GmbH), samples were centrifuged for 5 minutes at 12000 rpm. Supernatants were transferred into new tubes and after 10 minutes of incubation at room-temperature an equal volume of 70 V/V% ethanol was added into each tube.

Seroneutralization

Seroneutralization assay was performed on a selected serum sample set as previously described⁶². Sera were diluted in 7-point serial twofold dilution in triplicate in serum-free Dulbecco's Modified Eagle's Medium (DMEM, VWR®) in sterile 96-well microtiter plates. Positive and negative control sera were also applied (with and without serum for negative control). An equal volume of 60 ± 20 TCID50 NiV-Mal was added into each well and incubated for 1 hour on 37°C. After this step samples were transferred onto monolayer Vero E6 cells (approximately 1.8E + 05 cells/mL) maintained in serum-free DMEM in 96-well cell culture plates (TPP, Switzerland). The neutralizing antibody titers of each sample were determined by the lack of cytopathic effect (CPE) after a 5 days incubation in a 37°C CO₂ incubator. For triplicates the geometric mean of end dilutions was calculated and reported as a neutralizing antibody titer (Nab).

Cell lines

Human monocytic THP-1 cell lines WT, cGAS KO, STING KO or IFI16 KO were obtained from Veit Hornung lab (Mankan et al., 2014) and cultured in RPMI 1640 GlutaMAX supplemented with 10% heat-inactivated FBS, 1% HEPES and 1% penicillin-streptomycin mix. For infection, THP-1s were plated in 12-well plates at 5x10⁵ cells/well and cultured with rNiV-Malaysia-eGFP (NiV-M-eGFP) at a MOI of 0.3 or 1 or rMeV-EdmH-eGFP at a MOI of 0.1 or 1 for 48h.

Human pulmonary microvascular endothelial cells (HPMEC) 63 from a male donor were cultured in Endothelial Cell Growth Medium GM MV2 (Promocell) and SupplementalPack (5% FCS, 5 ng/ml recombinant hEGF, 10 ng/ml recombinant human bFGF, 20 ng/ml long R3 IGF, 0.5 ng/ml recombinant hVEGF, 1 µg/ml ascorbic acid), in flasks coated with 0.1% bovine gelatine (Sigma) in PBS. For infection, HPMECs were plated at 2.5×10^5 cells/well in 12-well plates or at 5×10^4 cells/well in 8-well lbidi slides and cultured with NiV-M-eGFP at a MOI of 0.3, 1 or 2 or MeV-EdmH-eGFP at a MOI of 1 PFUs/cell for 48 h.

293T cells (ATCC) were cultured in DMEM supplemented with 10% FBS, 1% HEPES and 1% penicillin-streptomycin. For transfection, 293T were plated in 24-well plates at $5x10^5$ cells/well. 16 h after transfection, 293T cells were co-cultured with 293 cells (ATCC) in 12-well plates for 24 h.

WT and phCMV-NiV-G or phCMV-NiV-F-transfected human adenocarcinoma epithelial cells (HeLa) were cultured in DMEM supplemented with 10% FBS, 1% HEPES and 1% penicillin-streptomycin. HeLa WT cells

were plated in 6-well plates at $5x10^5$ cells/well and then transfected with 2 µg phCMV.NiV-G or phCMV.NiV-F generated as previously described⁶⁴. Then cells were selected using G418 at 1 mg/ml before being cultured as described above. For microscope analysis, HeLa cells (ATCC) were plated in 8-well lbidi slides at $4x10^5$ cells/well and cultured for 48h before fixation. For immunoprecipitation, WT HeLa cells were plated in 6-well plates at $2.5x10^5$ cells/well and cultured with NiV-M-eGFP or MeV-EdmH-eGFP at a MOI of 0.3 for 48h. All cell types were incubated at 37°C with 5% CO2 and were tested negative for Mycoplasma spp.

Drugs

H-151, a specific inhibitor for STING (InvivoGen, Cat# inh-h151) and RU.521, a specific inhibitor for cGAS (InvivoGen, Cat# inh-ru521), were added 1 h before infection of HPMEC cells at 10 μ M and 10 μ g/ml, respectively, selected according to the previously published results ^{65,66}. Then, cells were infected with rNiV-eGFP and incubated for 48 h at 37°C with 5% CO2.

Fusion inhibitory peptides

Unconjugated MeV HRC peptide was purchased from Shanghai Ruifu Chemical Co., Ltd. Bis-maleimide cholesterol was custom made by Charnwood Molecular, Ltd. HRC4 was conjugated with cholesterol and purified as previously described ^{67,50}.

VIKI-PEG4-Chol fusion inhibitor peptide was produced by standard Fmoc-solid phase methods and cholesterol was attached to peptides as previously described ⁴⁹. Polyethylene glycol (PEG) was obtained from Quanta BioDesign (Plain City, OH).

Virus-specific fusion inhibitory peptides were diluted in culture medium and added 6h post infection or in correspondence to transfection at 2 μ M or 1 μ M.

RNA extraction and RT-qPCR

For mouse samples, total nucleic acid extraction was performed using QIAsymphony SP instrument with QIAsymphony DSP Virus/Pathogen Mini Kit and Complex200_OBL_V4_DSP protocol (QIAGEN GmbH, Hilden, Germany).

For in vitro experimentations, cells were collected at indicated time points and RNA extracted using appropriate NucleoSpin RNA Kits according to the manufacturer's instructions.

Equal amounts of extracted RNA (100 ng) were reverse transcribed using the iScript Select cDNA Synthesis Kit and amplified by real-time PCR using Platinum SYBR Green qPCR SuperMix-UDG on a StepOnePlus Real-Time PCR System. Pfaffl Model ⁶⁸ and Bustin MIQE checklist ⁶⁹ were used for all validations and calculations. To validate the efficacy of our primers, a PCR on a positive control (cDNA from corresponding stimulated cells) has been performed before dosing several dilutions of our PCR products using the Denovix DS-11-FX spectrophotometer to evaluate the quantity of DNA in each dilution.

Then, the PCR products were 10-fold serially diluted with a range from 10^{-1} to 10^{-12} to validate efficacy, specificity and sensitivity of each couple of primers used for qPCR. Moreover, the exact number of copies in each qPCR reaction was obtained by calculating the "N0 Samples = N0 Standard * Efficacy- Δ Ct" before being converted using molecular weight of each targeted gene and Avogadro number. Results obtained were converted to "copies/ μ g of RNA" for cell lysates. Finally, normalization was performed by dividing obtained numbers of RNA copies of the target genes with the deviation of the glyceraldehyde 3-phosphate dehydrogenase (GAPDH) used as house-keeping gene. Specific sets of primers were designed and validated for the detection of human hGAPDH, hIFN β , hCXCL-10 and hIL-6, murine mGAPDH, mCXCL-10 and mIFN β and viral NiV-N and MeV-N.

Immunohistochemistry

Brain, lung and spleen from mice were embedded in paraffin wax and sectioned at 7 μ m. Slides were deparaffinated and rehydrated in three Xylene baths for 5 min each, followed by two 100% alcohol baths for 5 min, and then succeeded with multiple baths using decreasing level of alcohol for 3 min each. After deparaffination, slides were put in a sodium citrate solution in a boiling water bath for 20 min for heat-induced epitope retrieval and washed 3 times in PBS for 3 min afterwards. Activity of endogenous peroxydase was blocked using a H_2O_2 0.3% solution. Blocking of non-specific epitopes is done using PBS-2.5% decomplemented Normal Horse Serum + 0.15% Triton X-100 for 30 min. Then, primary rabbit anti-NiV N antibody was used at 1/10000 dilution and incubated overnight at 4°C in the blocking buffer. For secondary antibody and revealing steps, ImmPress system (anti-rabbit ig/peroxydase) was used. Counterstaining was performed using Harris solution and photographs were taken with a microscope Zeiss Axiovert 100M.

Flow cytometry

THP-1 cells were seeded in 12-well plates at 2.5×10⁵ cells/well before being infected with NiV-eGFP and MeV-eGFP at a MOI of 0.3 or 0.1, respectively, and cultured for 48 h at 37°C with 5% CO2. Then, cells were washed with PBS 1X and fixed with methanol-free paraformaldehyde (PFA) 4% 15 minutes at 4°C. Afterwards, cells were reconstituted in PBS 1X and evaluated for eGFP expression using a Gallios flow cytometer in the BSL-4 or a 4L Fortessa flow cytometer. 293T transfected with or without NiV-F or NiV-G plated in 24-well plates and 293 cells prior to co-culture were detached by resuspension and transferred in polystyrene tubes. HeLa-NiV-F and HeLa-NiV-G cells were washed with PBS, detached with TrypLE 5–10 minutes at 37°C and transferred to polystyrene tubes after inactivating TrypLE with culture medium. 293T, 293 and HeLa were then washed 4 minutes at 1500 rpm with PBS 1X and incubated with primary anti-NiV-F or anti-NiV-G antibodies in PBS-1% fetal bovine serum (FBS) 30 minutes at 4°C. Cells were washed again before being incubated with II anti-mouse AF488-conjugated antibody in PBS-1% FBS 20 minutes at 4°C. Following two washes in PBS 1X, AF488 expression was measured using a 4L Fortessa flow cytometer.

Fluorescence microscopy

Following infections of THP-1 and HPMEC cells with NiV-eGFP and MeV-eGFP or transfection of 293T cells with eGFP, GFP fluorescence was visualized at Leica DMIRB microscope in BSL-4 or Eclipse Ts2R NIKON microscope in BSL-2.

Immunoblot analysis

Heated protein lysates were separated by SDS-PAGE in Any kD Mini-PROTEAN TGX Precast Protein Gels (Bio-Rad) and electro transferred for 7 minutes onto polyvinylidene difluoride (PVDF) membranes using Trans-Blot Turbo Transfer System and Trans-Blot Turbo Midi 0.2 µm PVDF Transfer Packs (Bio-Rad). PVDF membranes were blocked in Tris-buffered saline containing 10% milk for 1 h at room temperature and then incubated overnight at 4°C with the following primary antibodies diluted 1:1000 in TBS-0.1% Tween-0.5% milk: mouse anti-GAPDH (Millipore), rabbit anti-STING, rabbit anti-S366 p-STING, rabbit anti-p65, rabbit anti-phospho-p65, rabbit anti-cGAS (all Cell Signaling) and mouse anti-IFI16 (SCBT). Membranes were then washed 3 times using TBS-0.1% Tween and incubated 1 h at room temperature with horseradish peroxydase conjugated anti-mouse or anti-rabbit IgG antibodies (1:5000) or Trueblot antibodies (1:1000) diluted in TBS-0.1% Tween-0.5% milk. Membranes were then washed 3 times in TBS-0.1% Tween, once in TBS and incubated in Super Signal West Dura or in Super Signal West Femto reagent (Thermoscientific) for 1–3 minutes. Chemiluminescent signals were measured with the ImageQuant LAS 4000 Imaging System.

Transfection and co-culture

293T cells were plated in 24-well plates at $5x10^5$ cells/well and transfected with a mix of NiV-Mal-F and/or NiV-Mal-G, pCAGGS empty vector and eGFP plasmids using TranslT-LT1 kit according to the manufacturer's instructions. Right after transfection, cells were treated or not with VIKI fusion inhibitor peptide at 1 μ M and incubated overnight at 37°C and 5% CO₂. 293T were then washed twice with PBS 1X to eliminate residual plasmids in the supernatant and co-cultured with 293 cells (5X10⁵ cells/well) in 12-well plates for 24h prior to RNA extraction and qPCR.

Immunofluorescence

For HPMEC infections, 5x10⁴ cells were seeded in 8-well Ibidi slides before being infected with NiV-eGFP or MeV-eGFP at a MOI of 2 or 1, respectively, and cultured for 48 h at 37°C with 5% CO₂. For HeLa WT or HeLa-NiV-F and HeLa-NiV-G coculture, cells were plated at 4x10⁴ cells/well in 8-well Ibidi slides and incubated 48 h at 37°C with 5% CO₂. Cells were washed with PBS and stained with Mitotracker Orange 100 nM according to the manufacturer's instructions before undergoing fixation with PFA 4% 20 minutes at 4°C. Slides were permeabilized and blocked with a PermBlock solution (3% bovine serum albumin (BSA)-0.3% Triton X-100 in PBS 1X) for 30 minutes and incubated overnight at 4°C with the following primary antibodies: rabbit anti-phospho-STING (Cell Signaling), rabbit anti-phospho-histone H2A.X (Cell Signaling), mouse anti-cGAS (SCBT) or mouse anti-IFI16 (SCBT) diluted 1:100 in PermBlock solution. Slides were then washed 3 times with PBS 1X, incubated 1 h at room temperature with a mix of

fluorophore-conjugated secondary antibody (anti-rabbit AF647, anti-rabbit AF488 or anti-mouse AF488 all from Invitrogen) 1:750 and DAPI (Merck) 1:1000 in PermBlock. Finally, slides were washed 5 times with PBS 1X, covered with Fluoromount-G mounting medium (Invitrogen) and stored at 4°C. Fluorophore expression was evaluated using a Zeiss Axio OBSERVER Z.1 microscope in the BSL-4 or a Confocal ZEISS LSM800 microscope, and photographs were treated using ImageJ software version Java 1.8.0_112.

Cytoplasm extraction and immunoprecipitation

HeLa cells were plated in 6-well plates at 2.5×10^5 cells/well and infected with NiV-eGFP or MeV-eGFP at a MOI of 0.3. 6 hours post infection, cells were treated or not with VIKI or HRC4 fusion inhibitor peptides, respectively and incubated 48 h at 37°C with 5% $\rm CO_2$. Cells were washed with PBS 1X and detached with trypsin prior to cytosol extraction, which was performed using a CE buffer (HEPES 10 mM, KCl 60 mM, EDTA 1 mM, NP-40 0.075% V/V, DTT 1 mM and protease-phosphatase inhibitor 1 mM in PBS) adjusted to pH 7.6 according to Rockland's cytoplasm extraction protocol

(https://www.rockland.com/resources/nuclear-and-cytoplasmatic-extract-protocol/). Pellets were resuspended in 100 µl of CE buffer and incubated on ice for 3 minutes. Afterwards, cells were centrifuged and supernatants containing cytoplasmic extracts were transferred to new tubes. 500 µl of RIPA and protease-phosphatase inhibitor solution were added to cytoplasmic extracts and 100 µl of samples were kept to perform western blot analysis. The remaining sample was lysed in rotation 30 minutes at 4°C and centrifuged 10 minutes at 10000 rpm at 4°C. The supernatants were split in two, one half was incubated with rabbit anti-cGAS antibody (Cell Signaling) and the other with mouse anti-IFI16 antibody (SCBT) 1:100 2 h in rotation at 4°C. EZview™ Red agarose beads were added to the lysates and samples were incubated overnight at 4°C in rotation. Beads were pulled down by centrifugation 1 minute at 10000 rpm at 4°C and washed 3 times with RIPA buffer on ice. From each tube, 125 µl of immunoprecipitated product were mixed with LDS and reducing agent for western blot analysis and 375 µl underwent DNA extraction.

DNA extraction and qPCR

Immunoprecipitated agarose beads were washed with PBS 1X. 500 µl of NTI buffer from NucleoSpin Gel and PCR Clean-up kit (Macherey-Nagel) were added before heating samples 1 h at 60°C and DNA extraction was then performed according to manufacturer's instructions. DNA was then analyzed by qPCR using couples of primers specific for mitochondrial (mt) or nuclear (Nuc) DNA as described by Sato et al. (2021) and quantified as described above. The quantity of DNA was normalized on protein bands measured by densitometry, calculated as quantity of immunoprecipitated target over whole cell target over whole cell GAPDH. All values were expressed as fold change compared to the non-infected condition.

Quantification and statistical analysis

Flow cytometry analysis

The results are presented in the form of histograms representing the mean eGFP positive cells for each condition and error bars representing the standard error mean (SEM) for n = 6 experimental replicates. The different conditions were compared to the control (WT infected). Statistical significance was assessed by a one-way ANOVA, followed by a Tukey's multiple comparisons test; *p < 0.05, **p < 0.01, **p < 0.001 and **p < 0.0001 (threshold of significance of 5%).

qPCR analysis

The results are presented in the form of histograms, representing the mean of copies of mRNA for a gene for each condition and error bars representing the standard error mean (SEM). Points represent the number of experimental replicates. For experiments with n=3 replicates, statistical significance was assessed by non-parametric Kruskal-Wallis test and Conover's post-hoc test. For experiments with more than 3 replicates, statistical significance was assessed by t-test or one-way ANOVA, followed by a Tukey's multiple comparisons test; *p < 0.05, **p < 0.01, **p < 0.001 and **p < 0.0001 (threshold of significance of 5%).

Densitometry

Densitometric analyses of phospho-STING were performed using ImageJ 1.52p Fiji package software (https://imagej.net/Fiji). STING and GAPDH expression were used for normalization. The results are presented in the form of histograms and error bars represent the standard error mean (SEM) for n = 3 independent experiments. Statistical significance was assessed by t-test; *p < 0.05, **p < 0.01, **p < 0.001 and **p < 0.0001 (threshold of significance of 5%).

Image quantification

Fluorescence microscopy images were analyzed and quantified using QuPath-0.4.3 software (https://qupath.github.io/). In non-infected or fusion inhibitor-treated conditions, automatic segmentation was performed, allowing the measurement of mean intensity/cell or nuclear mean intensity/cell. In infected conditions, syncytia were manually selected and mean intensity of target fluorophore was divided by the number of nuclei inside the syncytium. The analysis was performed on n = 50 events on average for each of 4 independent replicates. The measurement of nuclear p65 fraction was performed on n = 32 events. Statistical significance was assessed by a one-way ANOVA, followed by Tukey's or Dunnett's multiple comparisons test; *p < 0.05, **p < 0.01, ***p < 0.001 and ****p < 0.0001 (threshold of significance of 5%).

Declarations

Data availability:

The data that support the findings of this study are available from the corresponding author upon reasonable request.

Acknowledgments:

We are grateful to all the members of the group Immunobiology of viral infection at CIRI, and Audrey Richard and Claudia Flippone from ERINHA, for the help in the realization of this study. We acknowledge the contribution of the SFR Biosciences (UMS3444/CNRS, US8/Inserm) in Lyon and CELPHEDIA Infrastructure (http://www.celphedia.eu/), and particularly the center AniRA flow cytometry facility and Lymic Platim center for microscopy. Graphical schemes were created with Biorender.

Funding:

The work was supported by INSERM, by Aviesan Sino-French agreement on Nipah virus study and by ERINHA-Advance project (funding from the European Union's Horizon 2020 Research & Innovation Program, grant agreement n. 824061).

Author contributions:

Conceptualization: MI, LA, BH

Investigation: LA, MI, CD, RP, OR, CM, JS, BP, DD, LK, JS

Supervision: MI, BH, KZ, UK

Writing—original draft: LA, MI

Writing-review & editing: LA, MI, BH, OR, CM, UK, JS

Competing interests:

Authors declare that they have no competing interests.

References

- 1. Ishikawa, H. & Barber, G. N. STING is an endoplasmic reticulum adaptor that facilitates innate immune signalling. *Nature* **455**, 674–678 (2008).
- 2. Hopfner, K.-P. & Hornung, V. Molecular mechanisms and cellular functions of cGAS-STING signalling. *Nat. Rev. Mol. Cell Biol.* **21**, 501–521 (2020).
- 3. Chen, C. & Xu, P. Cellular functions of cGAS-STING signaling. *Trends Cell Biol.* S0962-8924(22)00252-5 (2022) doi:10.1016/j.tcb.2022.11.001.
- 4. Gentili, M. *et al.* The N-Terminal Domain of cGAS Determines Preferential Association with Centromeric DNA and Innate Immune Activation in the Nucleus. *Cell Rep.* **26**, 2377-2393.e13 (2019).
- 5. Civril, F. et al. Structural mechanism of cytosolic DNA sensing by cGAS. Nature 498, 332–337 (2013).
- 6. Xia, P., Wang, S., Gao, P., Gao, G. & Fan, Z. DNA sensor cGAS-mediated immune recognition. *Protein Cell* **7**, 777–791 (2016).

- 7. Ergun, S. L., Fernandez, D., Weiss, T. M. & Li, L. STING Polymer Structure Reveals Mechanisms for Activation, Hyperactivation, and Inhibition. *Cell* **178**, 290-301.e10 (2019).
- 8. Dobbs, N. *et al.* STING Activation by Translocation from the ER Is Associated with Infection and Autoinflammatory Disease. *Cell Host Microbe* **18**, 157–168 (2015).
- 9. Tsuchiya, Y., Jounai, N., Takeshita, F., Ishii, K. J. & Mizuguchi, K. Ligand-induced Ordering of the Cterminal Tail Primes STING for Phosphorylation by TBK1. *EBioMedicine* **9**, 87–96 (2016).
- 10. Tanaka, Y. & Chen, Z. J. STING specifies IRF3 phosphorylation by TBK1 in the cytosolic DNA signaling pathway. *Sci. Signal.* **5**, ra20 (2012).
- 11. Panne, D., McWhirter, S. M., Maniatis, T. & Harrison, S. C. Interferon regulatory factor 3 is regulated by a dual phosphorylation-dependent switch. *J. Biol. Chem.* **282**, 22816–22822 (2007).
- 12. Schindler, C., Levy, D. E. & Decker, T. JAK-STAT Signaling: From Interferons to Cytokines *. *J. Biol. Chem.* **282**, 20059–20063 (2007).
- 13. Amurri, L., Horvat, B. & lampietro, M. Interplay between RNA viruses and cGAS/STING axis in innate immunity. *Front. Cell. Infect. Microbiol.* **13**, 1172739 (2023).
- 14. Aguirre, S. *et al.* DENV Inhibits Type I IFN Production in Infected Cells by Cleaving Human STING. *PLOS Pathog.* **8**, e1002934 (2012).
- 15. lampietro, M. *et al.* Control of Nipah Virus Infection in Mice by the Host Adaptors Mitochondrial Antiviral Signaling Protein (MAVS) and Myeloid Differentiation Primary Response 88 (MyD88). *J. Infect. Dis.* **221**, S401–S406 (2020).
- 16. lampietro, M. *et al.* Activation of cGAS/STING pathway upon paramyxovirus infection. *iScience* **24**, (2021).
- 17. Cox, R. M. & Plemper, R. K. Structure and organization of paramyxovirus particles. *Curr. Opin. Virol.* **24**, 105–114 (2017).
- 18. Pelissier, R., lampietro, M. & Horvat, B. Recent advances in the understanding of Nipah virus immunopathogenesis and anti-viral approaches. *F1000Research* **8**, 1763 (2019).
- 19. Chua, K. B. *et al.* Nipah virus: a recently emergent deadly paramyxovirus. *Science* **288**, 1432–1435 (2000).
- 20. Mougari, S., Gonzalez, C., Reynard, O. & Horvat, B. Fruit bats as natural reservoir of highly pathogenic henipaviruses: balance between antiviral defense and viral tolerance. *Curr. Opin. Virol.* **54**, 101228 (2022).
- 21. Soman Pillai, V., Krishna, G. & Valiya Veettil, M. Nipah Virus: Past Outbreaks and Future Containment. *Viruses* **12**, E465 (2020).
- 22. Laksono, B. M., de Vries, R. D., McQuaid, S., Duprex, W. P. & de Swart, R. L. Measles Virus Host Invasion and Pathogenesis. *Viruses* **8**, 210 (2016).
- 23. Guglielmi, G. Measles erases immune 'memory' for other diseases. *Nature* (2019) doi:10.1038/d41586-019-03324-7.

- 24. Amurri, L., Reynard, O., Gerlier, D., Horvat, B. & lampietro, M. Measles Virus-Induced Host Immunity and Mechanisms of Viral Evasion. *Viruses* **14**, 2641 (2022).
- 25. Suvvari, T. K. et al. The re-emergence of measles is posing an imminent global threat owing to decline in its vaccination rates amid COVID-19 pandemic: a special focus on recent outbreak in India a call for massive vaccination drive to be enhanced at global level. *Int. J. Surg. Lond. Engl.* 109, 198–200 (2023).
- 26. Francesco, D. & Antonia, M. Measles Resurgence in Europe: An Open Breakthrough in the Field of Vaccine-Preventable Diseases. *Pathogens* **12**, 1192 (2023).
- 27. Lee, B. Envelope-receptor interactions in Nipah virus pathobiology. *Ann. N. Y. Acad. Sci.* **1102**, 51–65 (2007).
- 28. Tatsuo, H., Ono, N., Tanaka, K. & Yanagi, Y. SLAM (CDw150) is a cellular receptor for measles virus. *Nature* **406**, 893–897 (2000).
- 29. de Swart, R. L. *et al.* Predominant infection of CD150+ lymphocytes and dendritic cells during measles virus infection of macaques. *PLoS Pathog.* **3**, e178 (2007).
- 30. Mühlebach, M. D. *et al.* Adherens junction protein nectin-4 is the epithelial receptor for measles virus. *Nature* **480**, 530–533 (2011).
- 31. Dörig, R. E., Marcil, A., Chopra, A. & Richardson, C. D. The human CD46 molecule is a receptor for measles virus (Edmonston strain). *Cell* **75**, 295–305 (1993).
- 32. Gerlier, D. *et al.* Efficient major histocompatibility complex class II-restricted presentation of measles virus relies on hemagglutinin-mediated targeting to its cellular receptor human CD46 expressed by murine B cells. *J. Exp. Med.* **179**, 353–358 (1994).
- 33. Aguilar, H. C., Henderson, B. A., Zamora, J. L. & Johnston, G. P. Paramyxovirus Glycoproteins and the Membrane Fusion Process. *Curr. Clin. Microbiol. Rep.* **3**, 142–154 (2016).
- 34. Gamble, A. *et al.* Drivers and Distribution of Henipavirus-Induced Syncytia: What Do We Know? *Viruses* **13**, 1755 (2021).
- 35. Sato, H. *et al.* Downregulation of mitochondrial biogenesis by virus infection triggers antiviral responses by cyclic GMP-AMP synthase. *PLoS Pathog.* **17**, e1009841 (2021).
- 36. Tsuchida, T. *et al.* The ubiquitin ligase TRIM56 regulates innate immune responses to intracellular double-stranded DNA. *Immunity* **33**, 765–776 (2010).
- 37. Zhang, J., Hu, M.-M., Wang, Y.-Y. & Shu, H.-B. TRIM32 Protein Modulates Type I Interferon Induction and Cellular Antiviral Response by Targeting MITA/STING Protein for K63-linked Ubiquitination. *J. Biol. Chem.* **287**, 28646–28655 (2012).
- 38. Balka, K. R. *et al.* TBK1 and IKKε Act Redundantly to Mediate STING-Induced NF-κB Responses in Myeloid Cells. *Cell Rep.* **31**, 107492 (2020).
- 39. Unterholzner, L. *et al.* IFI16 is an innate immune sensor for intracellular DNA. *Nat. Immunol.* **11**, 997–1004 (2010).

- 40. Dunphy, G. *et al.* Non-canonical Activation of the DNA Sensing Adaptor STING by ATM and IFI16 Mediates NF-κB Signaling after Nuclear DNA Damage. *Mol. Cell* **71**, 745-760.e5 (2018).
- 41. Goubau, D., Rehwinkel, J. & Reis e Sousa, C. PYHIN proteins: center stage in DNA sensing. *Nat. Immunol.* **11**, 984–986 (2010).
- 42. Chiang, C. & Gack, M. U. Post-translational Control of Intracellular Pathogen Sensing Pathways. *Trends Immunol.* **38**, 39–52 (2017).
- 43. Dhondt, K. P. *et al.* Type I interferon signaling protects mice from lethal henipavirus infection. *J. Infect. Dis.* **207**, 142–151 (2013).
- 44. Mathieu, C. *et al.* Lethal Nipah virus infection induces rapid overexpression of CXCL10. *PloS One* **7**, e32157 (2012).
- 45. Jahun, A. S. *et al.* Leaked genomic and mitochondrial DNA contribute to the host response to noroviruses in a STING-dependent manner. 2021.08.26.457800 Preprint at https://doi.org/10.1101/2021.08.26.457800 (2021).
- 46. Ren, H. *et al.* Micronucleus production, activation of DNA damage response and cGAS-STING signaling in syncytia induced by SARS-CoV-2 infection. *Biol. Direct* **16**, 20 (2021).
- 47. Ku, J. W. K. *et al.* Bacterial-induced cell fusion is a danger signal triggering cGAS-STING pathway via micronuclei formation. *Proc. Natl. Acad. Sci.* **117**, 15923–15934 (2020).
- 48. Mathieu, C. *et al.* Prevention of Measles Virus Infection by Intranasal Delivery of Fusion Inhibitor Peptides. *J. Virol.* **89**, 1143–1155.
- 49. Mathieu, C., Porotto, M., Figueira, T. N., Horvat, B. & Moscona, A. Fusion Inhibitory Lipopeptides Engineered for Prophylaxis of Nipah Virus in Primates. *J. Infect. Dis.* **218**, 218–227 (2018).
- 50. Reynard, O. *et al.* Nebulized fusion inhibitory peptide protects cynomolgus macaques from measles virus infection. *Nat. Commun.* **13**, 6439 (2022).
- 51. S, T., M, M., L, L., P, M. & V, H. In vitro identification of mitochondrial oxidative stress production by time-resolved fluorescence imaging of glioma cells. *Biochim. Biophys. Acta Mol. Cell Res.* **1865**, (2018).
- 52. Ito, H., Kanbe, A., Hara, A. & Ishikawa, T. Induction of humoral and cellular immune response to HBV vaccine can be up-regulated by STING ligand. *Virology* **531**, 233–239 (2019).
- 53. Ulrich-Lewis, J. T. *et al.* STING Is Required in Conventional Dendritic Cells for DNA Vaccine Induction of Type I T Helper Cell- Dependent Antibody Responses. *Front. Immunol.* **13**, 861710 (2022).
- 54. Liu, Z. *et al.* A pan-sarbecovirus vaccine induces highly potent and durable neutralizing antibody responses in non-human primates against SARS-CoV-2 Omicron variant. *Cell Res.* **32**, 495–497 (2022).
- 55. Jønsson, K. L. *et al.* IFI16 is required for DNA sensing in human macrophages by promoting production and function of cGAMP. *Nat. Commun.* **8**, 14391 (2017).
- 56. Herschke, F. *et al.* Cell-cell fusion induced by measles virus amplifies the type I interferon response. *J. Virol.* **81**, 12859–12871 (2007).

- 57. Khalfi, P. *et al.* Antagonism of ALAS1 by the Measles Virus V protein contributes to degradation of the mitochondrial network and promotes interferon response. *PLoS Pathog.* **19**, e1011170 (2023).
- 58. Xie, J. et al. Dampened STING-Dependent Interferon Activation in Bats. *Cell Host Microbe* **23**, 297-301.e4 (2018).
- 59. Sun, B. *et al.* Dengue virus activates cGAS through the release of mitochondrial DNA. *Sci. Rep.* **7**, 3594 (2017).
- 60. Müller, U. *et al.* Functional role of type I and type II interferons in antiviral defense. *Science* **264**, 1918–1921 (1994).
- 61. Jin, L. *et al.* MPYS is required for IFN response factor 3 activation and type I IFN production in the response of cultured phagocytes to bacterial second messengers cyclic-di-AMP and cyclic-di-GMP. *J. Immunol. Baltim. Md* 1950 **187**, 2595–2601 (2011).
- 62. M, I., S, B., A, D. & B, H. Mouse Models of Henipavirus Infection. *Methods Mol. Biol. Clifton NJ* **2682**, (2023).
- 63. Krump-Konvalinkova, V. *et al.* Generation of human pulmonary microvascular endothelial cell lines. *Lab. Investig. J. Tech. Methods Pathol.* **81**, 1717–1727 (2001).
- 64. Guillaume, V. *et al.* Nipah Virus: Vaccination and Passive Protection Studies in a Hamster Model. *J. Virol.* **78**, 834–840 (2004).
- 65. Chang, D. *et al.* Extracellular cyclic dinucleotides induce polarized responses in barrier epithelial cells by adenosine signaling. *Proc. Natl. Acad. Sci.* **117**, 27502–27508 (2020).
- 66. Hayden, L. *et al.* Lipid-specific IgMs induce antiviral responses in the CNS: implications for progressive multifocal leukoencephalopathy in multiple sclerosis. *Acta Neuropathol. Commun.* **8**, 135 (2020).
- 67. Ft, B. *et al.* Inhibition of Measles Viral Fusion Is Enhanced by Targeting Multiple Domains of the Fusion Protein. *ACS Nano* **15**, (2021).
- 68. Pfaffl, M. W. A new mathematical model for relative quantification in real-time RT-PCR. *Nucleic Acids Res.* **29**, e45 (2001).
- 69. Bustin, S. A. *et al.* The MIQE guidelines: minimum information for publication of quantitative real-time PCR experiments. *Clin. Chem.* **55**, 611–622 (2009).

Figures

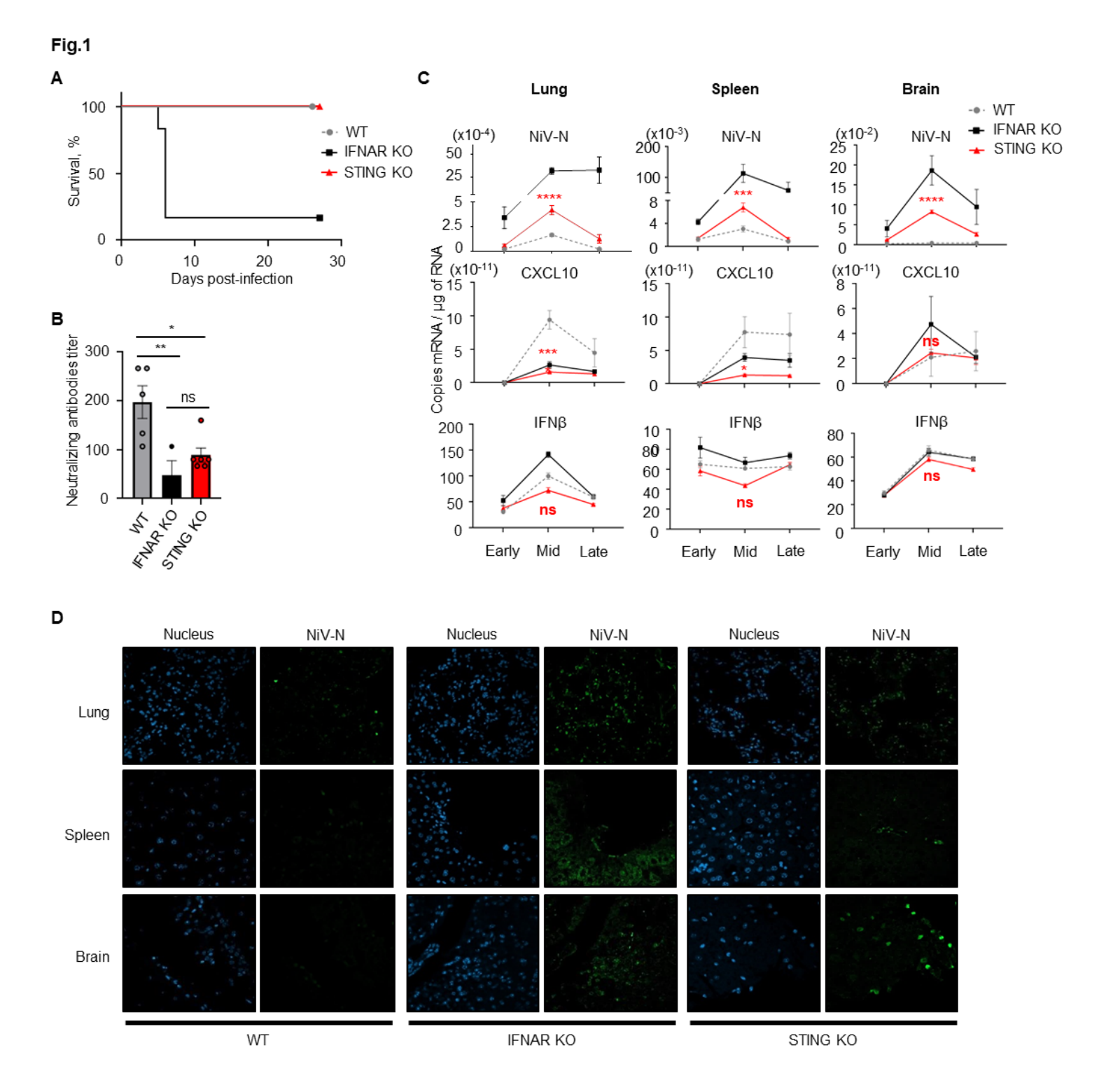


Figure 1

STING plays a role in the control of NiV infection in mice. (A) Wild-type (WT), IFN α/β receptor (IFNAR) KO and STING KO C57BL/6 mice were infected intraperitoneally with 106 plaque-forming unit (PFU) of NiV-Malaysia (NiV) and observed during 28 days post-infection. For kinetics analysis, results were grouped into early (from day 0+4h to day 2 post infection), mid (from day 2 to day 7) and late (from day 7 to day 28) phase of infection (6 animals per group). Survival of NiV-infected mice was followed up for 28 days (5 animals per group). (B) α -NiV neutralizing antibodies titer measured in serum of 5 WT mice euthanized

at day 28, 3 IFNAR KO mice euthanized at day 7 or day 27 and 6 STING KO mice euthanized at day 28. (C) NiV nucleoprotein (NiV-N), CXCL10 and IFNβ mRNA levels in murine lungs, spleens and brains harvested at early, mid or late phase were assessed by RT-qPCR. Data are represented as mean ± standard error of the mean (SEM). The difference between STING KO and WT was analyzed using one-way analysis of variance or two-way analysis of variance, followed by Tukey multiple comparison test: ns (not significant); *p<0.05; ***p<0.001; ****p<0.0001 compared to WT condition. (D) Lungs, spleens and brains of WT, IFNAR KO and STING KO C57BL/6 mice were harvested at day 7 post NiV infection and analyzed by fluorescence microscopy after staining with DAPI and anti-NiV-N antibody.

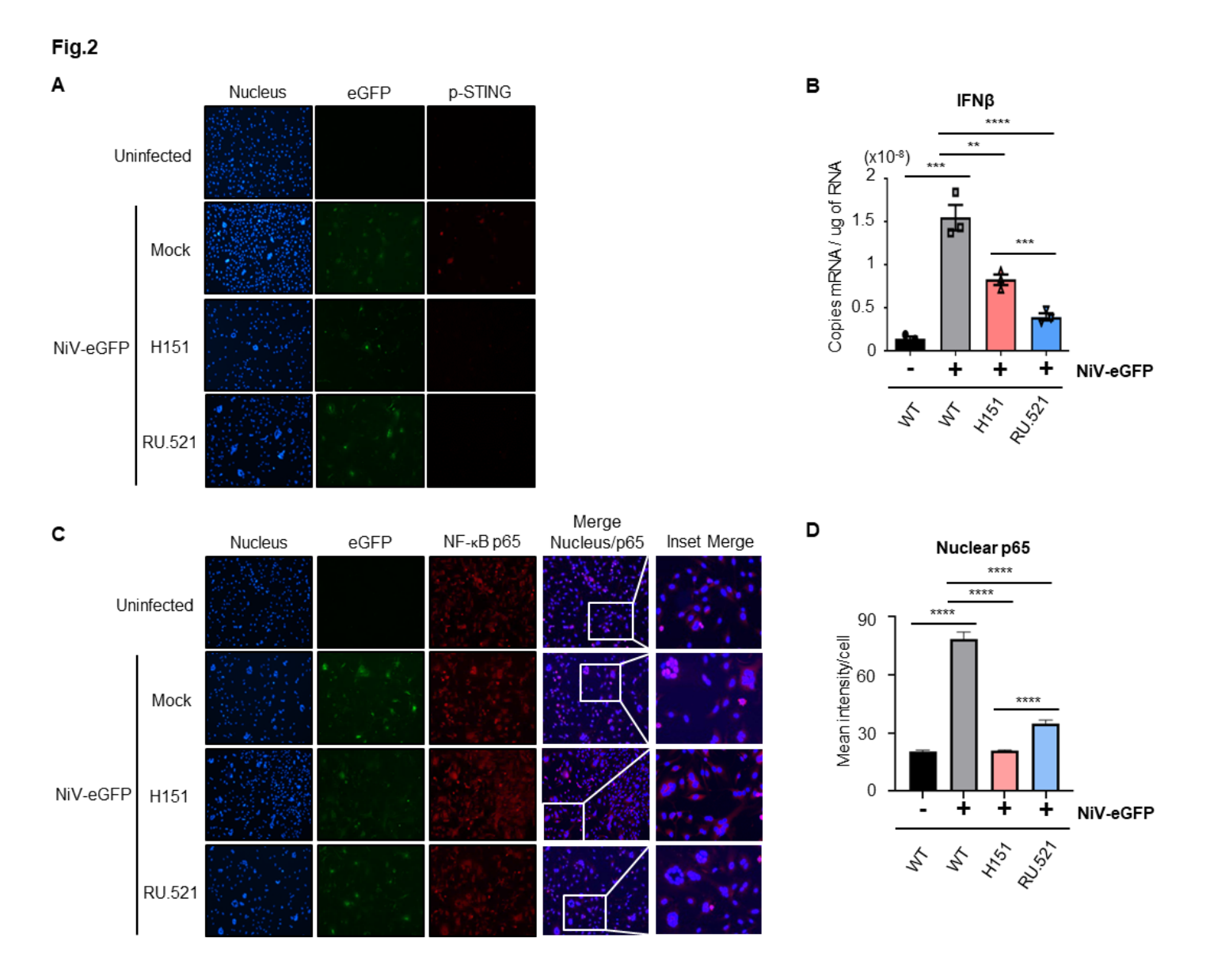


Figure 2

STING pathway controls IFNβ and NF-κB responses following NiV infection. Human pulmonary microvascular endothelial cells (HPMEC) were infected with NiV-eGFP at a MOI of 0.3 for 48h and treated or non-treated with a STING inhibitor (H151) or a cGAS inhibitor (RU.521) at 10 µM or 10 µg/ml, respectively, 1h before infection. (A,C) Cells were analyzed by fluorescence microscopy following fixation

and immunofluorescence staining of phospho-STING (p-STING) and NF- κ B p65. (B) Cells were harvested and analyzed by RT-qPCR for IFN β expression. Data from 3 independent experiments are represented as mean \pm SEM. All samples were analyzed using Kruskal-Wallis and Conover post-hoc test, *p<0.05; **p<0.01; ****p<0.0001 compared to NiV-infected WT condition. (D) The mean intensity of nuclear p65 fraction/cell was calculated using QuPath-0.4.3. For infected mock condition, only cells inside syncytia were analyzed (n=32). For uninfected and infected treated conditions, at least 250 events per condition were analyzed. Data are represented as mean \pm SEM. All samples were analyzed using one-way analysis of variance, followed by Tukey's multiple comparison test, *p<0.05; ****p<0.0001 compared to NiV-infected WT condition.

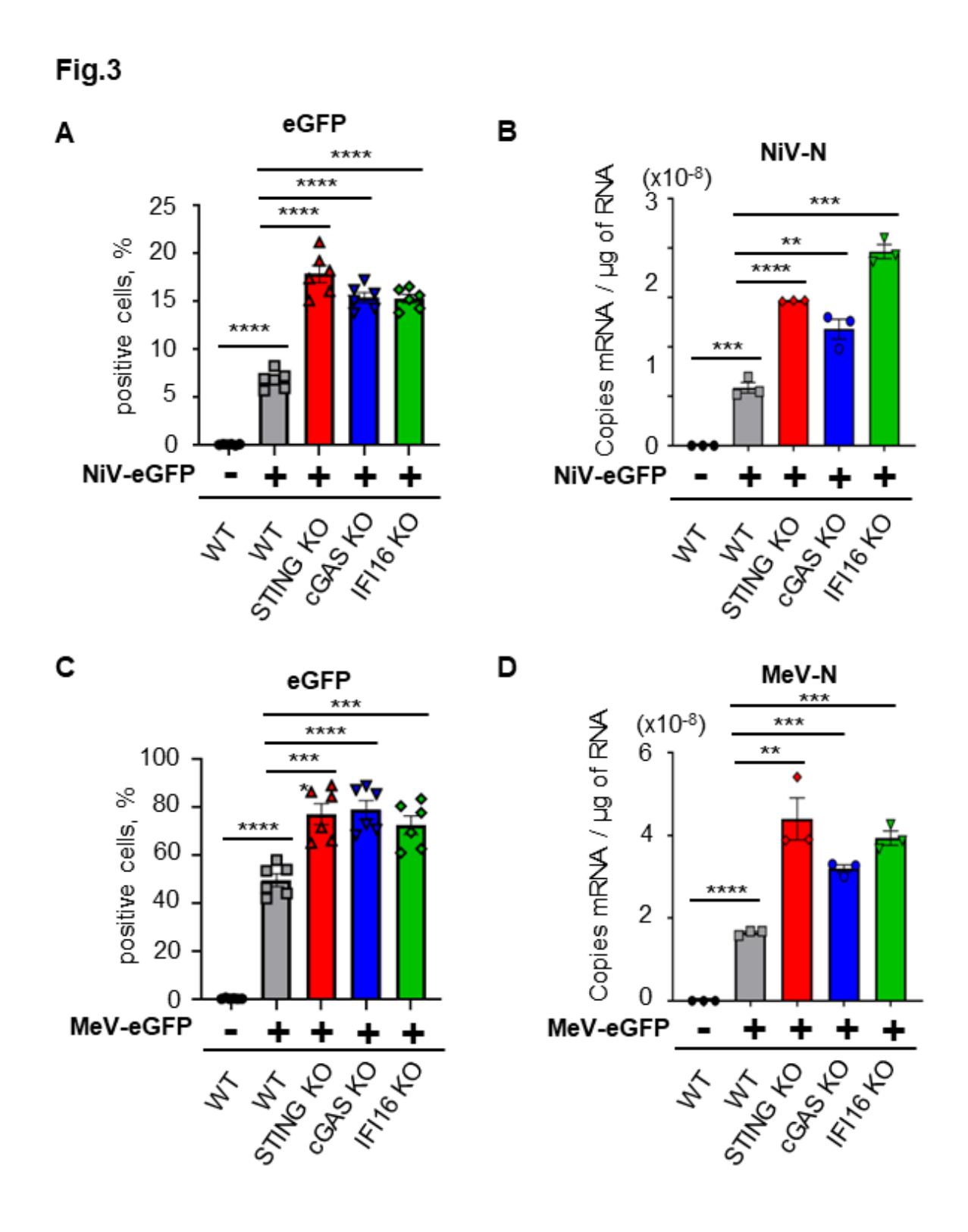


Figure 3

STING-associated sensors cGAS and IFI16 are involved in the control of NiV and MeV infection. WT, STING KO, cGAS KO or IFI16 KO THP-1 cells were infected with NiV-eGFP at a MOI of 0.3 or MeV-eGFP at a MOI of 0.1 for 48h. (A,C) eGFP expression was evaluated by flow cytometry in NiV-eGFP (A) or MeV-eGFP (C) infected cells (n=6). Data are represented as mean ± SEM. All samples were analyzed using one-way analysis of variance, followed by Tukey's multiple comparison test, ***p<0.001; ****p<0.0001

compared to NiV- or MeV-infected WT condition. (B,D) Cells were harvested and analyzed by RT-qPCR for NiV-N (C) or MeV-N (D) expression (n=3). Data are represented as mean ± SEM. All samples were analyzed using Kruskal-Wallis and Conover post-hoc test, ***p<0.001; ****p<0.0001 compared to NiV- or MeV-infected WT condition.

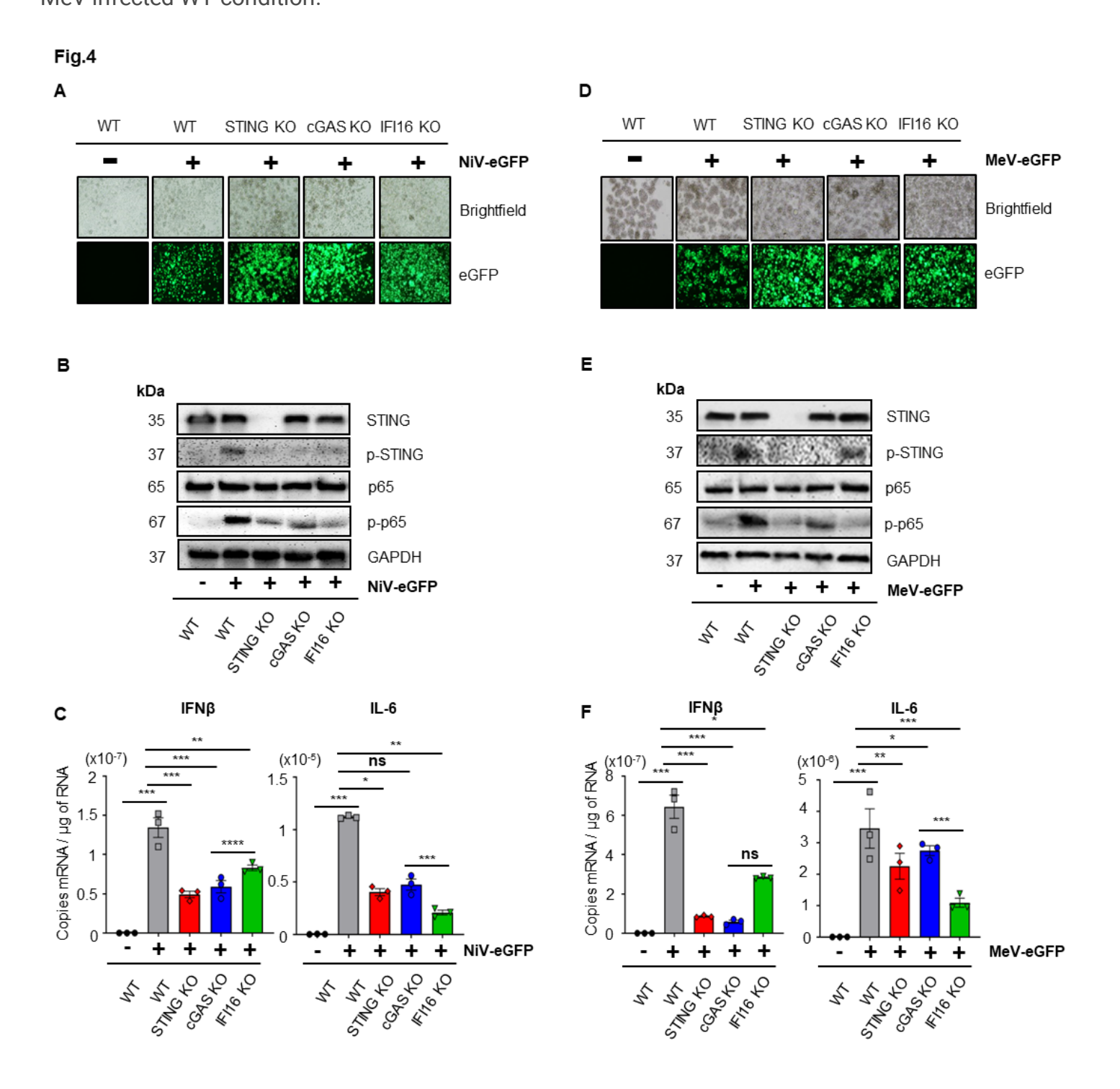


Figure 4

cGAS promotes phosphorylation of STING and IFI16 favors NF-кВ p65 activation following NiV and MeV infection. WT, STING KO, cGAS KO or IFI16 KO THP-1 cells were infected with NiV-eGFP (A-C) or MeV-eGFP (D-F) at a MOI of 1 for 48h. (A,D) Representative image of eGFP expression from 3 independent

experiments, evaluated by fluorescence microscopy in NiV- (A) and MeV- (D) infected cells. (B,E) NiV- (B) and MeV- (E) infected cells were analyzed for NF- κ B p65, phospho-p65 (p-p65), STING, phospho-STING (p-STING) and GAPDH expression by western blot analysis. (C,F) NiV- (C) or MeV- (F) infected cells were harvested and analyzed by RT-qPCR for IFN β and IL-6 expression (n=3). Data are represented as mean \pm SEM. All samples were analyzed using Kruskal-Wallis and Conover post-hoc test, **p<0.01; ***p<0.001; ****p<0.0001 compared to NiV- or MeV-infected WT condition.

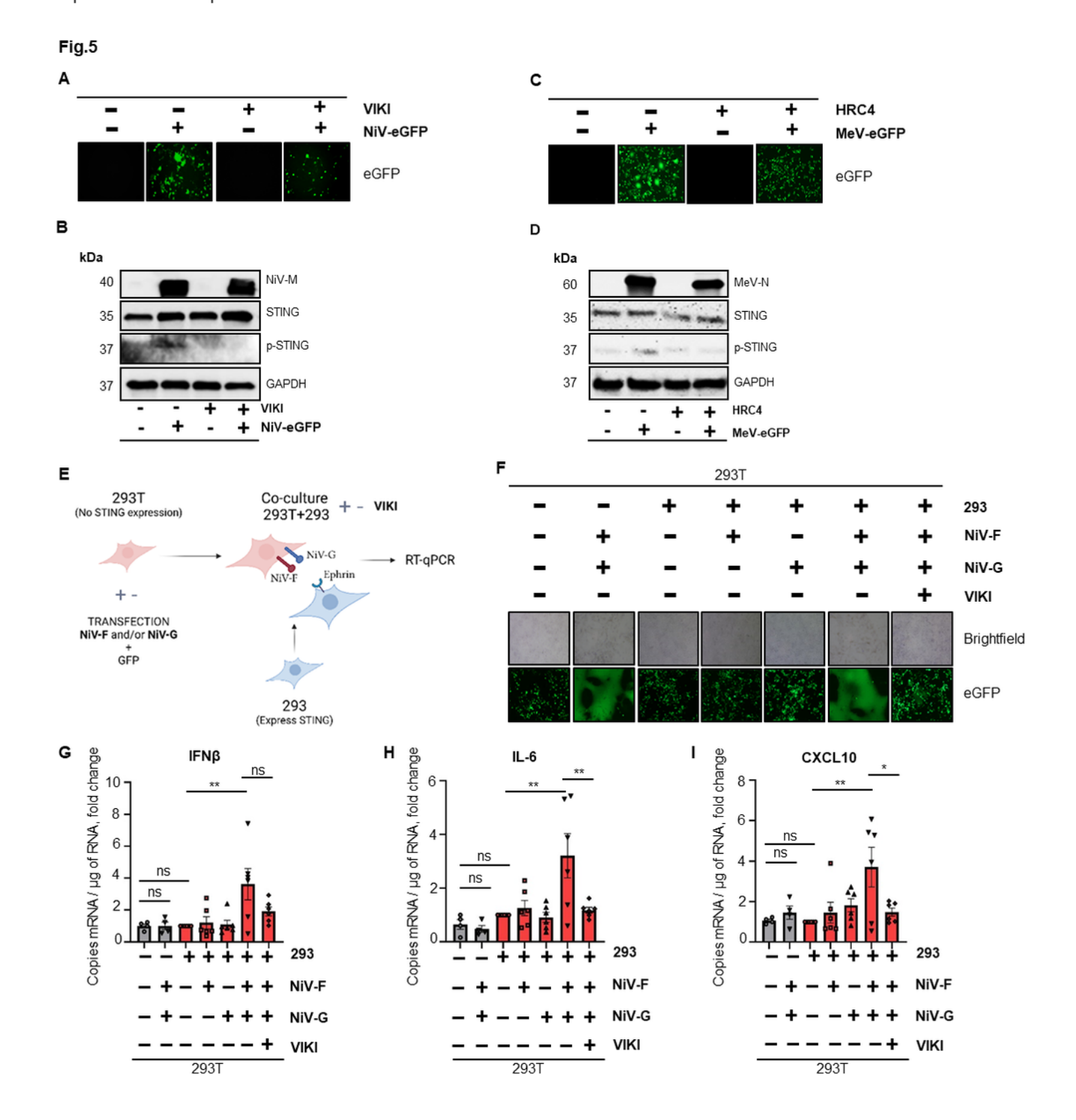


Figure 5

Viral-induced syncytia lead to STING activation and expression of IFN-I and inflammatory cytokines. (A-F) HPMEC cells were infected with NiV-eGFP at a MOI of 3 (A-B) or MeV-eGFP at a MOI of 1 (C-D) for 48h and treated or non-treated with VIKI or HRC4 fusion inhibitor peptides, respectively, at 2 μ M 6h post infection. (A,C) eGFP expression was evaluated by fluorescence microscopy on NiV- (A) or MeV- (C) infected cells. (B,D) Cells were analyzed for NiV-M or MeV-N, STING, p-STING and GAPDH expression by western blot analysis (B,D). (E-I) 293T cells were treated or non-treated with VIKI at 1 μ M, transfected with NiV-F and/or NiV-G and eGFP in presence or absence of empty vector and incubated overnight (E). 293T cells were then washed with PBS and co-cultured with 293 cells for 24h before undergoing RT-qPCR analysis. (F) eGFP expression and syncytia formation were evaluated by fluorescence microscopy. (G-I) Cells were harvested and analyzed by RT-qPCR for IFN β , IL-6 and CXCL10 expression. Data from 293T (n=4) and co-culture of 293T and 293 (n=6) are represented as mean \pm SEM and expressed as fold change compared to co-culture + empty vector condition. All samples were analyzed using one-way analysis of variance, followed by Tukey's multiple comparison test, *p<0.05; **p<0.01; ****p<0.001.

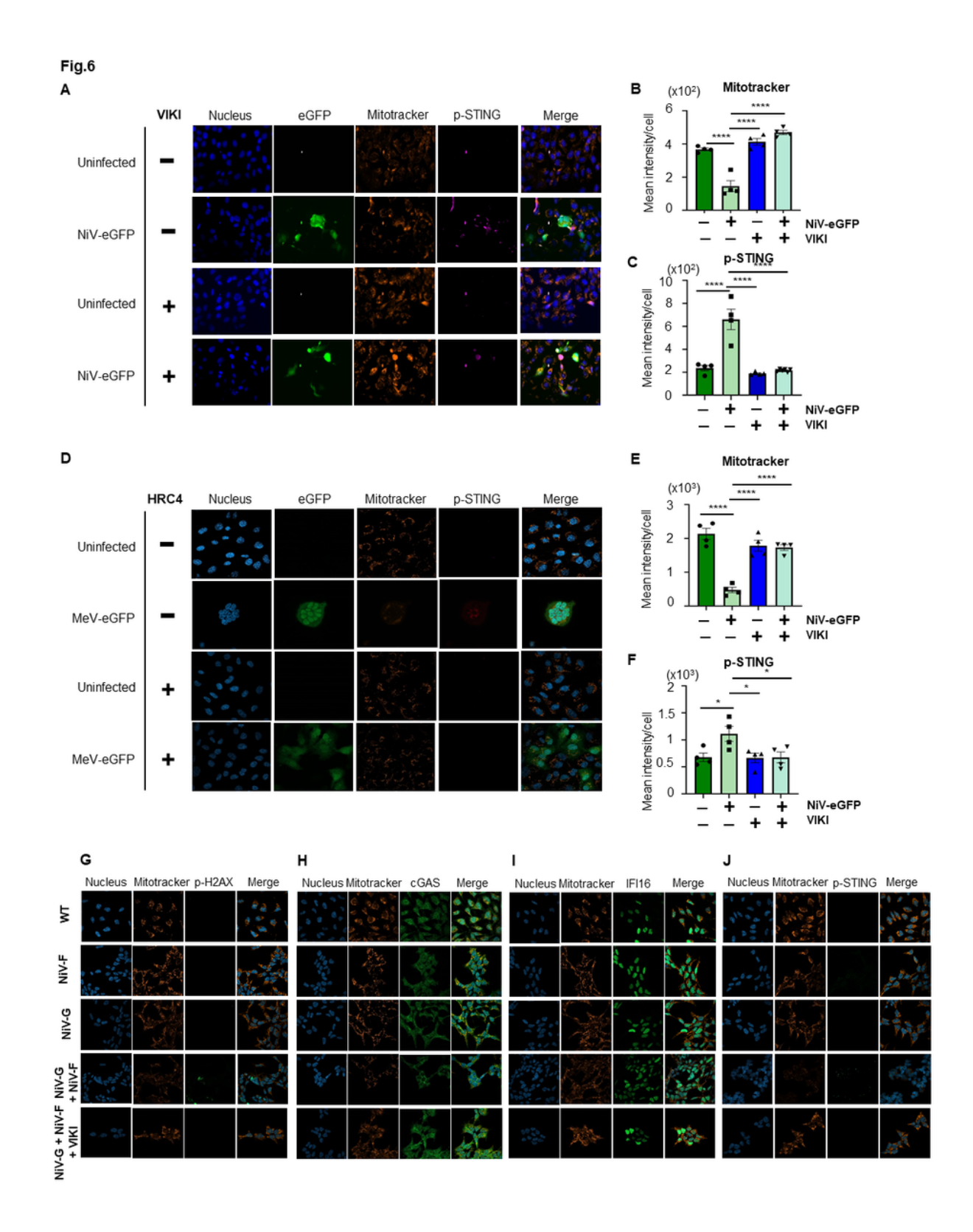


Figure 6

STING axis activation is associated with mitochondrial stress and DNA damage following paramyxovirus-induced syncytia formation. (A-F) HPMEC cells were infected with NiV-eGFP at a MOI of 3 (A-C) or MeV-eGFP at a MOI of 1 (D-F) for 48h and treated or non-treated with VIKI or HRC4 fusion inhibitor peptides, respectively, at 1 μ M (n=4). (A,D) NiV- (A) or MeV- (D) infected cells were stained with Mitotracker Orange 100 nM, fixed, stained with anti-p-STING antibody and analyzed by fluorescence

microscopy. (B, C, E, F) The mean fluorescence intensity per cell of Mitotracker (B, E) or p-STING (C, F) staining was calculated using QuPath-0.4.3 on at least 50 events per condition from each of for 4 independent replicates. For infected mock condition, only cells inside syncytia were analyzed. Data are represented as mean ± SEM. All samples were analyzed using one-way analysis of variance, followed by Dunnett's multiple comparison test, *p<0.05; ****p<0.0001 compared to NiV- or MeV-infected WT condition. (G-J) HeLa cells WT or stably expressing NiV-F or NiV-G were cultivated individually or co-cultured, treated or non-treated with VIKI fusion inhibitor peptide at 1 μM and incubated for 48h (n=3). Cells were stained with Mitotracker Orange at 100 nM, fixed, stained with anti-phosphorylated histone 2AX (p-H2AX) (G), anti-cGAS (H), anti-IFI16 (I) or anti-p-STING (J) antibodies and analyzed by confocal microscopy.

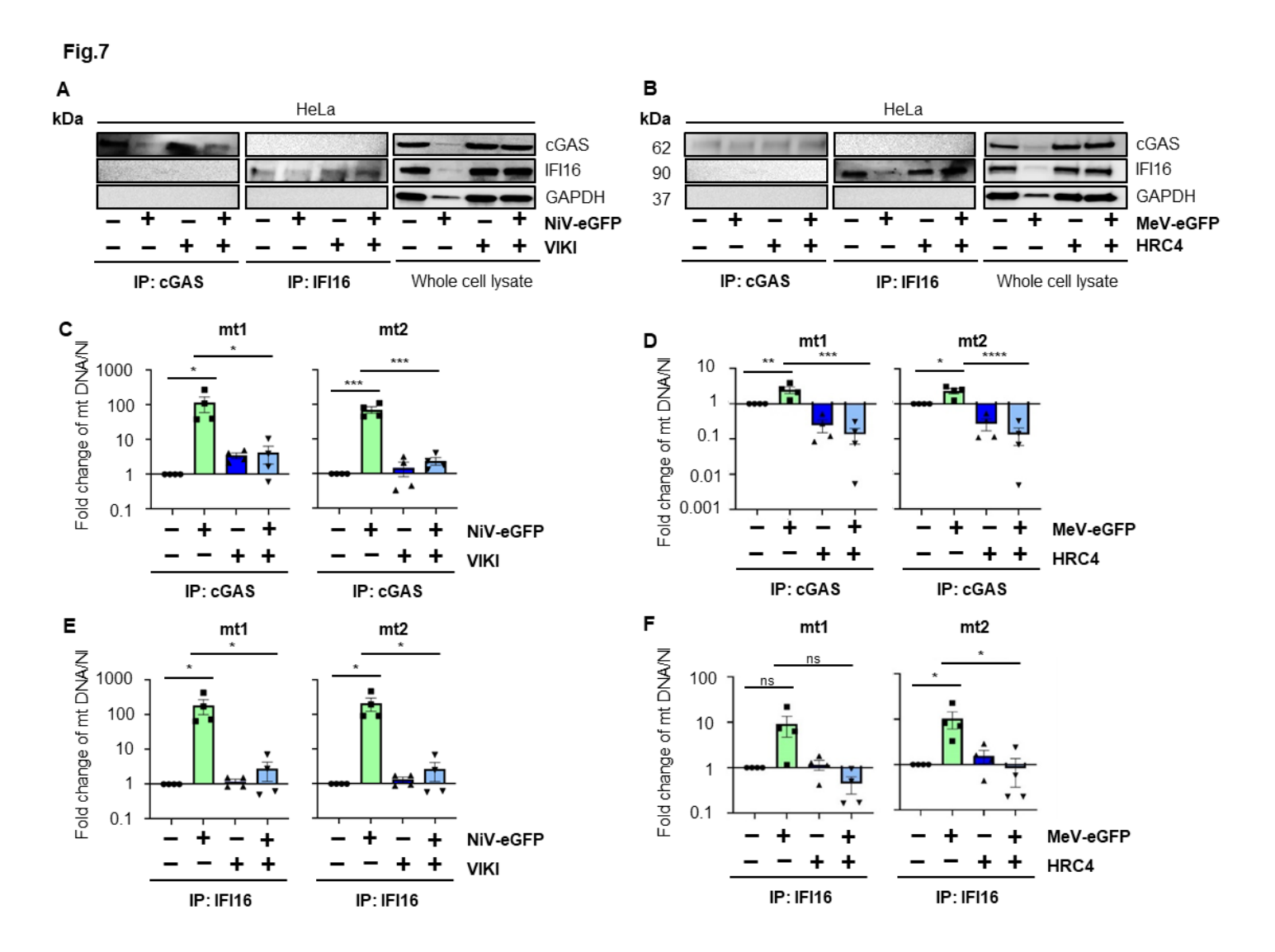


Figure 7

Mitochondrial DNA is responsible for STING activation through its sensing by both cGAS and IFI16 during NiV and MeV infection. HeLa cells were infected with NiV-eGFP (A-C) or MeV-eGFP (D-F) at a MOI of 0.3 and treated or not with VIKI or HRC4 fusion inhibitor peptides, respectively, at 1 μ M 6h post infection (n=4). 48h post infection, cytoplasm was extracted and cGAS and IFI16 proteins were

immunoprecipitated from cytoplasmic extract. DNA was purified from the immunoprecipitated products and analyzed by qPCR using primers specific for mtDNA. (A,B) Immunoprecipitated cGAS and IFI16 and whole cell lysates from NiV- (A) and MeV- (B) infected cells were analyzed for cGAS, IFI16 and GAPDH expression by western blot. (C-F) Purified DNA from immunoprecipitated cGAS (C, D) or IFI16 (E, F) was analyzed by qPCR for two mitochondrial (mt1 and mt2) DNA regions. Data are represented as mean ± SEM. All samples were analyzed using one-way analysis of variance, followed by Dunnett's multiple comparison test, *p<0.05; ***p<0.001 compared to NiV-infected WT condition.

Fig.8

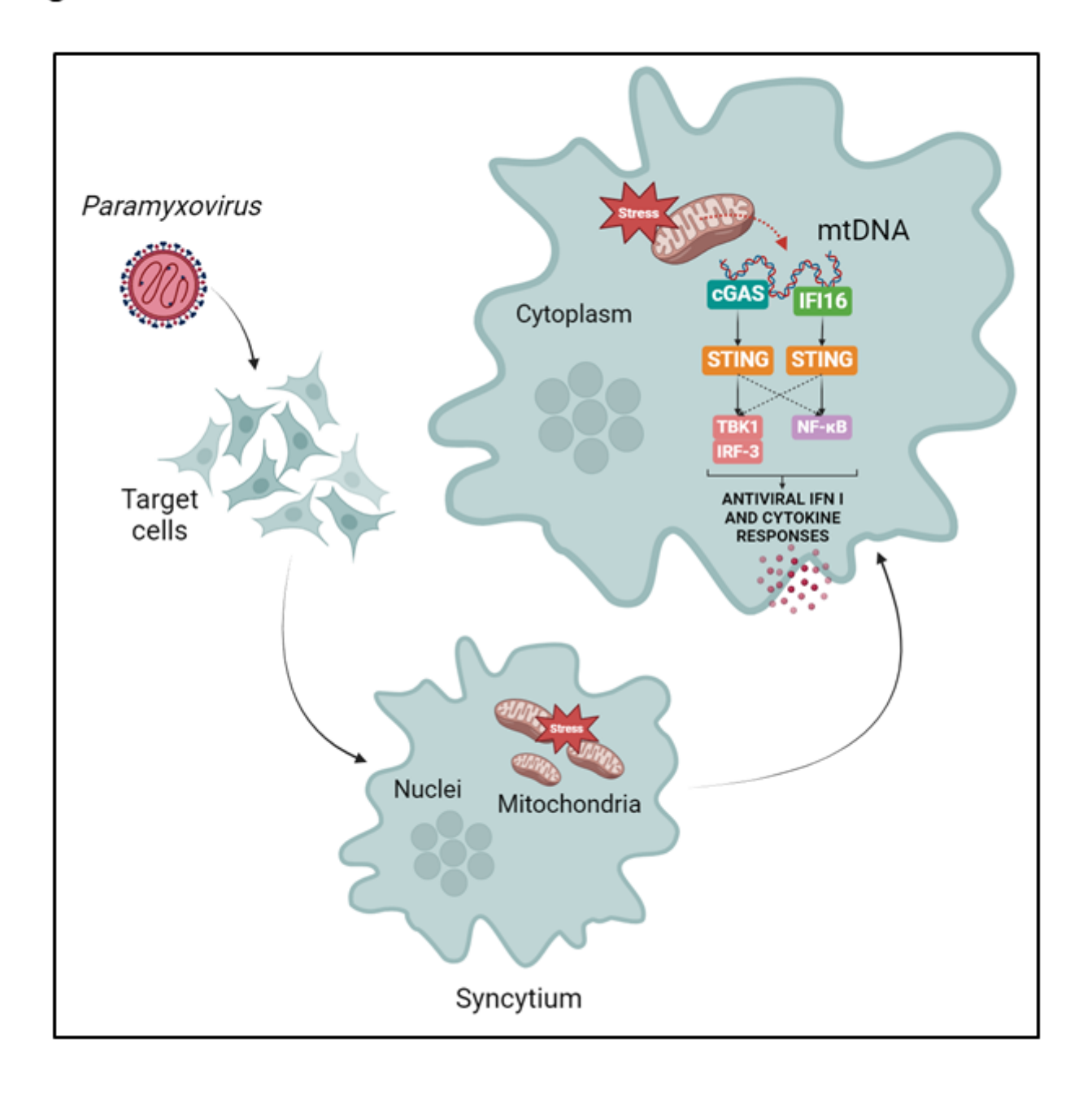


Figure 8

Schematic model representing the mechanisms responsible for STING activation following Nipah and Measles virus infection. Paramyxovirus infection provokes the structural rearrangement of target cells into multi-nucleated giant cells (syncytia), leading to mitochondrial stress induction. As a consequence of mitochondrial stress, mitochondrial DNA (mtDNA) is released in cytoplasm and detected by both cGAS and IFI16 intracellular DNA sensors. While cGAS preferentially activates STING/TBK1/IRF-3 axis leading to IFN-I response induction, IFI16 primarily activates STING/NF-κB and inflammatory cytokines response, which may altogether play a role in the antiviral protection.

Supplementary Files

This is a list of supplementary files associated with this preprint. Click to download.

• SupplementarymaterialsSTINGpaperNatCommv5.pdf